

1 Impact of urban environment on Savonius wind turbine performance: a  
2 numerical perspective

3 Riccardo Longo<sup>\*b,a</sup>, Patricia Nicastro<sup>c</sup>, Matteo Natalini<sup>c</sup>, Paolo Schito<sup>d</sup>, Riccardo Mereu<sup>c</sup>, Alessandro  
4 Parente<sup>a,e</sup>

5 <sup>a</sup>Université Libre de Bruxelles - Aéro-Thermo-Mécanique Department

6 <sup>b</sup>Politecnico di Milano - Dipartimento di Chimica, Materiali ed Ingegneria Chimica "G. Natta"

7 <sup>c</sup>Politecnico di Milano - Dipartimento di Energia

8 <sup>d</sup>Politecnico di Milano - Dipartimento di Meccanica

9 <sup>e</sup>Combustion and Robust Optimization Group (BURN), Université libre de Bruxelles and Vrije Universiteit Brussel, Bruxelles, Belgium

---

---

10 **Abstract**

11 In this study, computational fluid dynamics (CFD) is employed to evaluate the influence of surrounding  
12 buildings on the performance of a roof-mounted, 2-bladed Savonius vertical-axis wind turbine (VAWT). The  
13 latter is planned to be located in the Bovisa Campus of Politecnico di Milano. In the present work a pre-  
14 liminary simulation campaign has been conducted, explicitly depicting the surrounding area and employing  
15 an advanced Reynolds-averaged Navier-Stokes (RANS) model. This closure is suitable for Atmospheric  
16 Boundary Layer (ABL) simulation, reliably reproducing the various ground roughness elements and em-  
17 ploying a Building Influence Area (BIA) for a more accurate representation of the disturbed flowfield. After  
18 considering twelve main wind directions, the resulting velocity profiles are extracted and used as inlet con-  
19 ditions for a second session of simulations, related to the wind turbine.  
20 The final goal is to reproduce the effect of the surrounding buildings and to accurately forecast the en-  
21 ergy production of the machine. This is a relevant aspect of the increasingly topical framework of smart  
22 city, implying the exploitation of wind energy. Outcomes indicate that the resulting energy production of  
23 the machine remarkably departs from ideal conditions and that accounting for the surrounding topography  
24 becomes an aspect of great relevance.

\*Corresponding authors' emails: riccardo.longo@ulb.ac.be

\*\*Present address: Av. F.D. Roosevelt 50, 1050 Bruxelles-Belgique

Declarations of interest: none

## <sup>25</sup> Keywords

- <sup>26</sup> Urban wind energy generation; Renewable Energy; Vertical-axis wind turbine; Atmospheric boundary  
<sup>27</sup> Layer; Computational Fluid Dynamics; Sustainable built environment.

## <sup>28</sup> Nomenclature

Symbol	Description
$A_x$	BIA attenuation parameter
$C_1, C_2$	constant in the $k$ inlet profile
$C_\mu, C_{\epsilon 1}, C_{\epsilon 2}, \sigma_\epsilon$	constants in the $k - \epsilon$ model
$C_m, C_d, C_l, C_p$	torque, drag, lift and power coefficient for wind turbine
$E$	annual energy yield, $J$
$F_S$	safety factor
$f_c$	Coriolis parameter, $rad/s$
$f_i$	relative frequency during the year
$h$	ABL height, $m$
$H_n, H_{max}$	building's heights, $m$
$k$	turbulent kinetic energy, $m^2 s^{-2}$
$p$	pressure, $Nm^{-2}$
$p_c$	order of convergence
$P_{avail}$	available power, $W$
$r_h$	coarsening ratio
$S$	strain-rate invariant
$S_\epsilon$	source term in the $\epsilon$ equation
$\vec{u}$	wind velocity vector, $m s^{-1}$
$U$	mean streamwise wind speed, $m s^{-1}$
$U_p$	wind speed at first cell centroid, $m s^{-1}$
$U_{ref}$	reference wind speed, $m s^{-1}$
$U_{inf}$	reference wind turbine speed, $m s^{-1}$
$u_*$	ABL friction velocity, $m s^{-1}$

$x, y, z$	stream-wise, width and height coordinates, $m$
$\tilde{y}^+, y^+$	non-dimensional wall distances
$z_0$	aerodynamic roughness length, $m$
$\delta_u, \delta_k, \delta_\epsilon, \delta_h$	local deviation of turbulent properties
$\delta_*$	deviation in the sinusoidal simulation
$\epsilon$	turbulent dissipation rate, $m^2 s^{-3}$
$\kappa$	von Karman constant
$\mu_t$	dynamic turbulent viscosity, $kg m^{-1} s^{-1}$
$\omega$	specific rate of dissipation, $s^{-1}$
$\Omega$	vorticity invariant
$\rho$	density, $kg m^{-3}$

## **29 1. Introduction**

30 Energy sector researches and investments are more and more focused on renewable energy, in a frame-  
 31 work where decentralization is playing an important role [1, 2, 3, 4, 5]. In this scenario, small wind turbines  
 32 are one of the most promising solutions [6]; currently, Savonius vertical-axis wind turbines (VAWT) are  
 33 still not widespread, but their simplicity and better performance in disturbed flowfields, compared to small  
 34 horizontal-axis wind turbines (HAWT) make them a good alternative for distributed generation devices in  
 35 urban environment [7, 8].  
 36 CFD can be successfully employed to provide detailed information on the urban flowfield [9, 10]. In this re-  
 37 gard, Reynolds-averaged Navier–Stokes two-equation models can still offer a good compromise between  
 38 accuracy of results and computational time [11, 12, 13]. However, when applied with the standard wall  
 39 treatment, the conventional Richard and Hoxey [14] inlet profiles suffer from horizontal inhomogeneity  
 40 [15, 16, 17]. One of the reasons for the decay of the turbulence profiles lies in the inconsistency be-  
 41 tween the fully developed inlet profiles and the rough wall formulation [16, 18, 19]. Moreover, buildings  
 42 introduce swirl and recirculation zones that are not accurately reproduced by the standard two-equation  
 43 models [20, 21, 16, 17, 22].  
 44 To address these issues and to reproduce more realistic inlet conditions at a reasonable computational  
 45 cost, this study employs the comprehensive approach [23, 18, 16]. This model was designed for undis-  
 46 turbed flowfield, aiming to employ realistic inlet conditions and to solve the inconsistencies related to neutral

<sup>47</sup> atmospheric boundary layer (ABL); it was developed together with a wall treatment which is consistent with  
<sup>48</sup> the model's equations [18].

<sup>49</sup> Further advances are needed to extend the turbulence treatment to the case of disturbed flowfields: Longo  
<sup>50</sup> et al. [16, 17] employed different Non-Linear Eddy-Viscosity (NLEV) models inside an automatically de-  
<sup>51</sup> tected Building Influence Area (BIA), outperforming the standard RANS two equations models, with en-  
<sup>52</sup> hanced sensitivity to curvature, swirl and recirculation zones [21, 16, 22, 21, 20]. In the present work, all  
<sup>53</sup> the aforementioned turbulence improvements have been implemented in OpenFOAM®. Moreover, a new  
<sup>54</sup> concept of BIA is introduced to accurately detect the disturbance produced by the presence of buildings.  
<sup>55</sup> The resulting turbulence model is validated over three wind tunnel test cases and one real-scale case,  
<sup>56</sup> provided with experimental data. Subsequently, it is employed on the Bovisa Campus, considering twelve  
<sup>57</sup> wind directions.

<sup>58</sup> The resulting flow pattern will aerodynamically characterize the location selected for the wind turbine. The  
<sup>59</sup> subsequent step will be the coupling between the ABL simulations on the Bovisa Campus and the wind  
<sup>60</sup> turbine simulations. The turbulence conditions in the target location will be extrapolated and employed as  
<sup>61</sup> inlet conditions for the wind turbine simulation.

<sup>62</sup> Literature about Savonius VAWT studies includes both wind tunnel tests and numerical simulations. Typi-  
<sup>63</sup> cally, the first ones are mostly focused on the optimization of the blade shape [24] and consist in wind tunnel  
<sup>64</sup> test measurements [25] at different tip-speed ratio (TSR), overlap ratios and aspect ratios or even multiple  
<sup>65</sup> stage designs [26, 27]). In this regard, CFD studies can be mainly classified considering 2D and 3D inspec-  
<sup>66</sup> tion methods. 3D methods are preferable, being more consistent with experimental results [28, 29, 30]; the  
<sup>67</sup> majority of those studies consists in validation processes for different RANS turbulence models, among  
<sup>68</sup> which the Shear Stress Transport  $k - \omega$  (SST  $k - \omega$ ) is one of the most reliable.

<sup>69</sup> One of the main obstacles to the deployment of this technology is the gap between the forecast and actual  
<sup>70</sup> energy production. This can be related to the fact that real operating conditions are frequently not consid-  
<sup>71</sup> ered: these are affected by the surrounding environment [31, 32, 33] which, in the case of urban context,  
<sup>72</sup> is strongly case-dependent.

<sup>73</sup> In the last decades, few studies concerning building interactions with wind turbines have been carried  
<sup>74</sup> out, considering simplified building models [34] and neglecting the neighbour building's influence on wind  
<sup>75</sup> stream [35]. In the present work, the built environment around the target building is explicitly depicted and  
<sup>76</sup> a turbulence model accounting for the main ABL features is employed to represent the local flowfield and  
<sup>77</sup> realistically forecast the operating conditions of the machine. The results indicate that the location selected

78 on the target building is suitable for wind energy exploitation and that surrounding environment is playing a  
 79 non-negligible role on the efficiency of the wind turbine energy production. Conducting the same analysis  
 80 with the ideal inlet conditions would have led to a severe misprediction of the energy production of the  
 81 machine.

## 82 **2. ABL turbulence modelling**

83 Considering its feasibility and robustness, the  $k - \epsilon$  model remains one of the most common RANS closures  
 84 for ABL simulations [36, 37, 38, 39, 40]. However, when applied in its standard form, it suffers from several  
 85 drawbacks: overprediction of turbulent kinetic energy in stagnation regions, mis-representation of recircula-  
 86 tion zones and insensitivity of shear stress to the curvature [21, 41, 42, 43]. Moreover, a rise of stream-wise  
 87 gradients in the vertical profiles of turbulent quantities is generally observed if the inlet conditions are not  
 88 properly selected and they are not consistent with the wall treatment [17, 19]. For these reasons, an ad-  
 89 vanced/consistent ABL  $k - \epsilon$  model, validated in a number of studies [44, 23, 18, 16, 45, 46], is employed,  
 90 guaranteeing the reduction of the horizontal inhomogeneity in the inlet profiles, addressing the problem of  
 91 erroneous representation of disturbed flow regions and properly treating the various roughness elements.

### 92 **2.1. Undisturbed and disturbed flowfield treatment**

93 The comprehensive approach [23, 18, 16] is a turbulence model suitable for undisturbed flowfield. It con-  
 94 sists in the combination of appropriate boundary conditions, fulfilling ABL experimental data evidence and  
 consistent with the wall treatment (Table 1).

Table 1: Set of inlet conditions and turbulence variables for the comprehensive approach [17].

Inlet Conditions	Turbulence Model
$U = \frac{u_*}{\kappa} \ln \left( \frac{z+z_0}{z_0} \right)$	$\mu_t = C_\mu \rho \frac{k^2}{\epsilon}$
$k(z) = C_1 \ln(z + z_0) + C_2$	$S_\epsilon(z) = \frac{\rho u_*^4}{(z+z_0)^2} \left( \frac{(C_{\epsilon 2} - C_{\epsilon 1}) \sqrt{C_\mu}}{\kappa^2} - \frac{1}{\sigma_\epsilon} \right)$
$\epsilon(z) = \frac{u_*^3}{\kappa(z+z_0)}$	$C_\mu = \frac{u_*^4}{k^2}$

95  
 96 When dealing with disturbed flowfields a different modelling strategy has to be considered [16]. In this  
 97 regard, one possible solution is represented by NLEV models [21, 20, 22] which can accurately catch the  
 98 streamline curvature and swirl of a perturbed flowfield, thanks to the inclusion of quadratic and cubic terms

99 to the stress-strain relation and to the employment of a  $C_\mu$  depending on the local strain-rate and vorticity  
 100 invariants. The NLEV model selected for this study is the one proposed by Ehrhard and Moussiopoulos  
 101 [22], which defines  $C_\mu$  as:

$$C_\mu = \min \left[ \frac{1}{0.9S^{1.4} + 0.4\Omega^{1.4} + 3.5}, 0.15 \right] \quad (1)$$

102  
 103 The NLEV model is automatically employed whenever a disturbed flowfield is detected, through the adop-  
 104 tion of a Building Influence Area [23, 17, 16]. The BIA is identified using a local deviation parameter  $\delta$  that  
 105 estimates the relative error between homogeneous ABL conditions and the local values of relevant turbu-  
 106 lence parameters.

107 In this work, the BIA concept is further improved, combining three different deviations in the so-called hybrid  
 108 BIA. More precisely, the maximum of three local deviations ( $u - k - \epsilon$ ) is assigned to the cell and defines  
 109 the hybrid blending parameter  $\delta_h$ , which reads:

$$\delta_h = \max [\delta_u, \delta_k, \delta_\epsilon] \quad (2)$$

110 For a generic turbulent variable  $x$ , the deviation reads:

$$\delta_x = \min \left[ A_x \left| \frac{x_{wake} - x_{ABL}}{x_{ABL}} \right|, 1 \right] \quad (3)$$

111  $A_x$  is an attenuation parameter, meant to limit the unnecessary over-extent of the BIA. Turbulent kinetic  
 112 energy and turbulent dissipation rate are, by nature, more abrupt and scattering quantities, compared  
 113 to velocity. Their variability affects, consequently, the respective relative deviation. For this reason, the  
 114 attenuation parameters recursively employed are:  $A_u = 1$ ,  $A_k = 0.1$  and  $A_\epsilon = 0.1$ . Their calibration was  
 115 successfully validated on the basis of different wind tunnel and real scale test cases (some of them are  
 116 located in the supplementary material), all provided with experimental data [17, 47, 48, 45, 46];  $x_{wake}$  is  
 117 the local turbulence parameter value,  $x_{ABL}$  is the undisturbed value. If the flowfield is undisturbed, the  
 118 resulting deviation is zero:  $\delta_x = 0$ . On the contrary, a fully perturbed region would bring to a maximum  
 119 deviation:  $\delta_x = 1$ . The behavior of the blending approaches is explained in Table 2, where the BIA extent  
 120 is shown for four primitive geometries. These are the building blocks for many other shapes/forms. The  
 121 deviation  $\delta_h$  is then used to blend the comprehensive approach and the NLEV model parameters between  
 122 the undisturbed ABL and the BIA through a proper transition function [23, 49].

<sub>123</sub> Further information about the BIA metrics and the turbulent model employed in this study can be found in  
<sub>124</sub> [23, 16] and in the supplementary material.

<sub>125</sub> Similarly to Montazeri et al. [50], Longo et al. [16] compared the ABL model against a number of other  
<sub>126</sub> RANS approaches, proving the enhancement in accuracy of the proposed approach with respect to different  
<sub>127</sub> turbulence methodologies.

## Building Influence Area

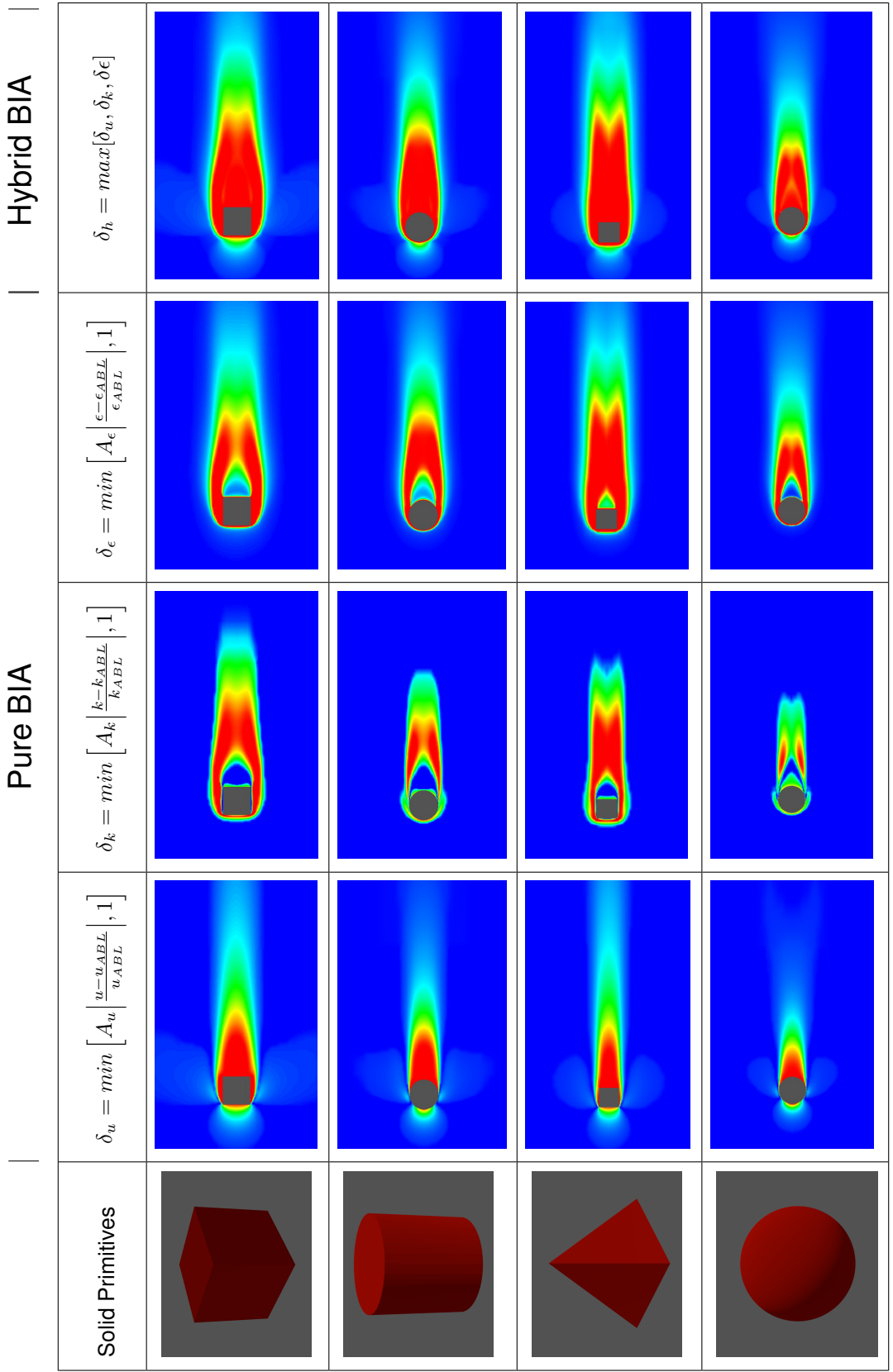


Table 2: Metric and extent of the BIA for the pure blending, based on the local deviation of  $u$ ,  $k$  and  $\epsilon$ , and hybrid blending, displayed on the horizontal plane for four primitive shapes: cube, cylinder, pyramid and sphere. The blue color represents a completely undisturbed flowfield, while the red one indicates a completely perturbed one. For all the geometries, the BIA metrics differently identify the disturbed areas and their combination in the Hybrid BIA results in the most exhaustive detection.

## 128 2.2. Validation of the ABL turbulence model

129 The Case B displays a 4:4:1 shaped building from the wind tunnel tests performed by Tominaga et al. [51],  
 130 displayed in Figure 1. The proposed ABL approach and the standard  $k - \epsilon$  model are compared against  
 the experimental data.

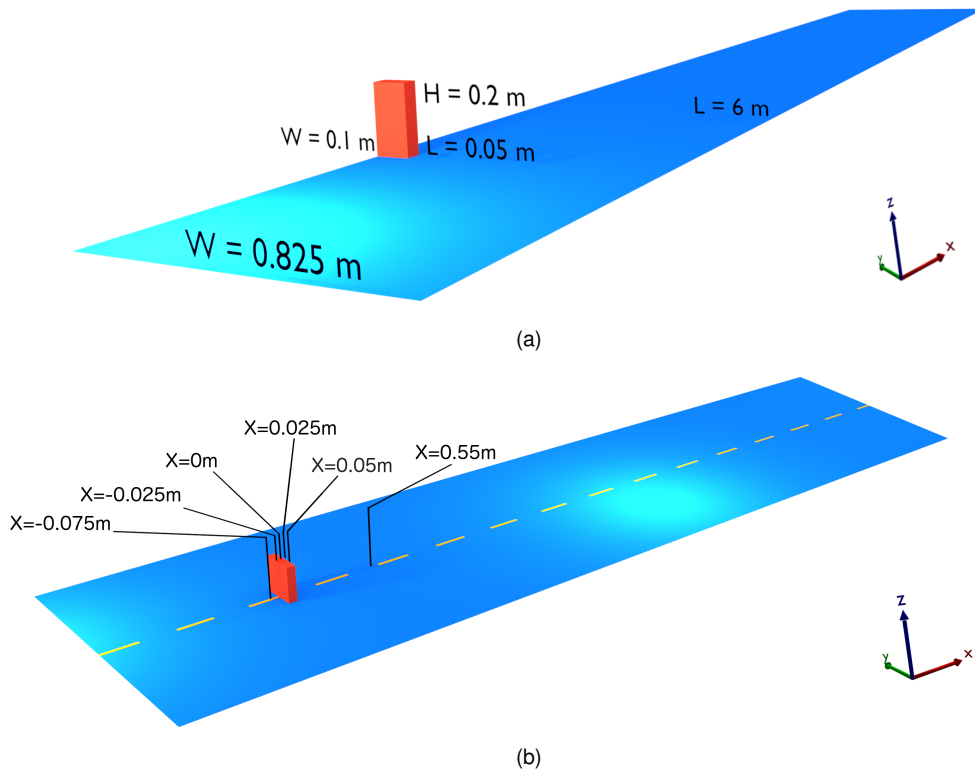


Figure 1: View, geometry (a) and vertical measurement lines (b) of the Case B from the Architectural Institute of Japan [51].

131 A mesh of 2 millions cells (330x78x78 hexa elements) was generated. Considering the symmetry of the  
 132 model with respect to the plane  $y = 0m$ , only half of the domain was studied, resulting in: length  $L = 6m$ ,  
 133 width  $W = 0.825m$  and height  $H = 1.6m$ . As shown in Figure 2, the mesh is finer close to the building and  
 134 to the ground boundaries, gradually decreasing in resolution once moving away from the region of interest.  
 135 As for the dimensionless wall distance, its values ranged between 50 and 190 all over the domain. A grid  
 136 sensitivity analysis was carried out, building one finer grid, consisting of 3.2 million cells ( $r_h = 1.18$ ), with a  
 137 resulting  $y^+$  ranging between 40 and 155. A conservative safety factor,  $F_S = 3$ , was employed. A GCI of  
 138 2% was determined both for  $u$  and  $k$ , with respect to the finest grid.  
 139 The roughness lenght  $z_0$  is equal to  $0.000096m$ . From Figures 3, it is possible to observe that the velocity  
 140 prediction is improved applying the ABL approach. This can be witnessed in Figure 3 (a-b-c-d), where the  
 141

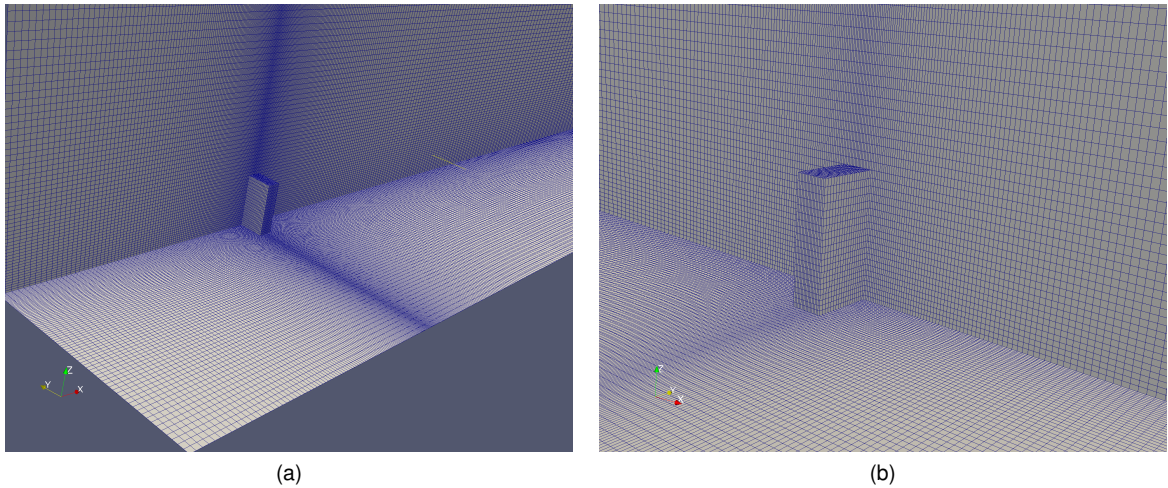


Figure 2: Computational mesh on the building, ground and symmetry surfaces for the Case B, from upwind (a) and downwind (b) views

- <sup>142</sup> upwind recirculation zone and the separation bubble above the building are better reproduced.
- <sup>143</sup> As for  $k$ , its overproduction is reduced by the employment of the BIA. This is evident when considering
- <sup>144</sup> Figure 4, especially at the impinging side of the building, with the standard  $k - \epsilon$  over-predicting turbulent
- <sup>145</sup> kinetic energy up to 500%.

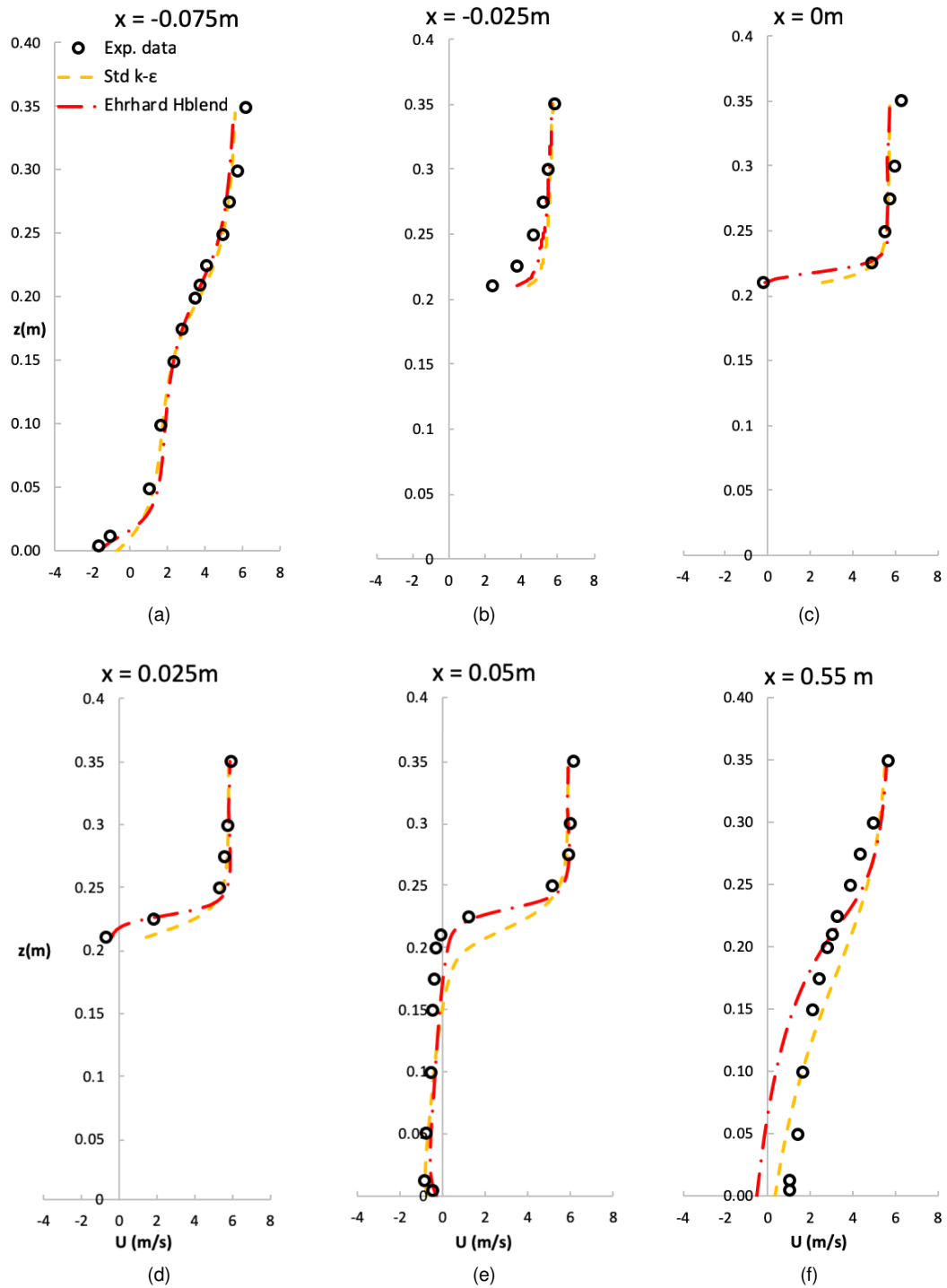


Figure 3: Comparison of experimental and numerical predictions of x-velocity for the Case B test case [51] at different locations of the domain, employing the standard  $k - \epsilon$  model and the proposed ABL turbulence approach.

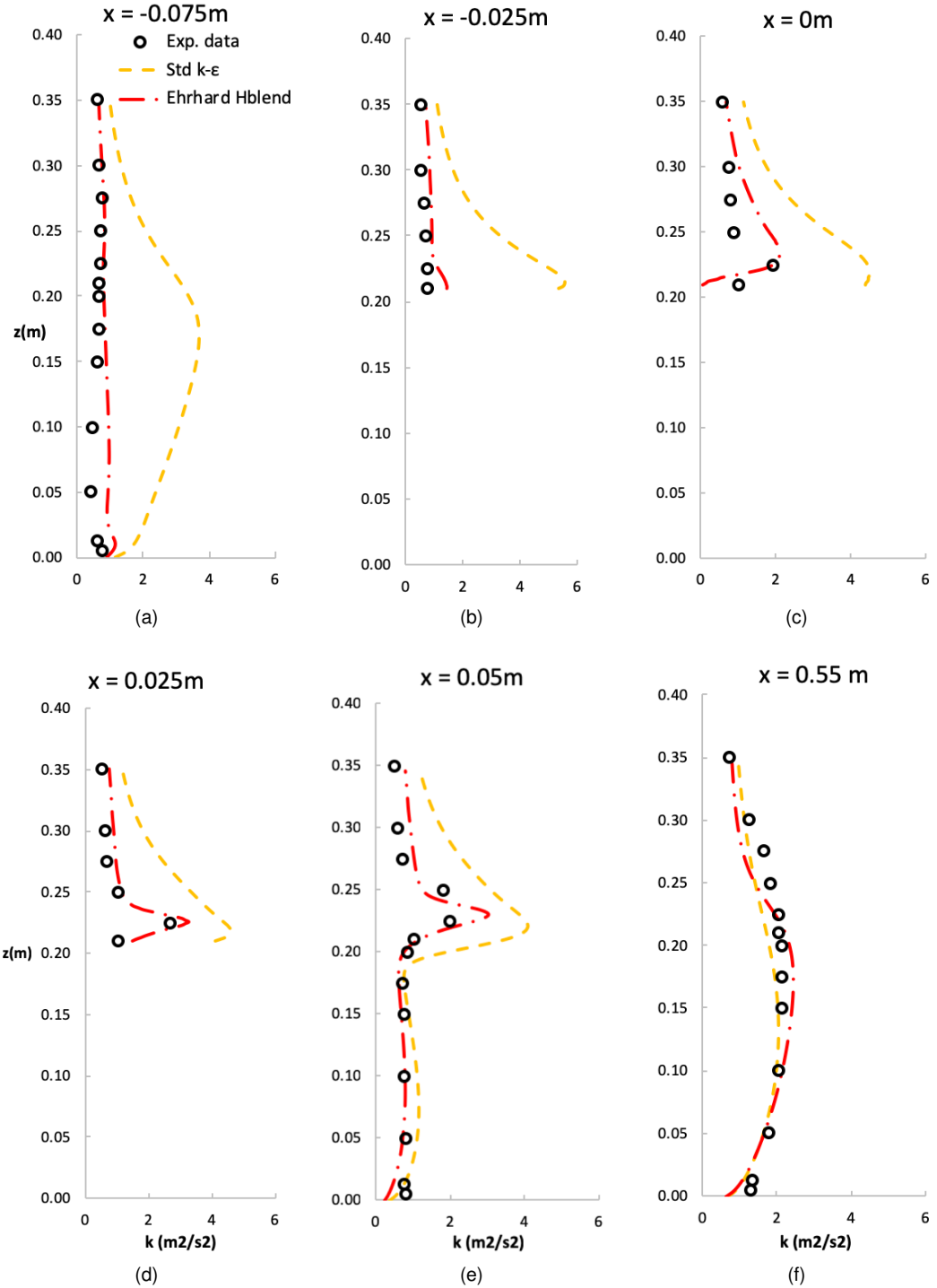


Figure 4: Comparison of experimental and numerical predictions of turbulent kinetic energy for the Case B test case [51] at different locations of the domain, employing the standard  $k - \epsilon$  model and the proposed ABL turbulence approach.

## **146 2.3. Urban Modelling Guidelines**

**147** Guidelines for domain sizing and mesh building can be found in Franke et al. [36, 52] and Tominaga et al.  
**148** [53]. The main guidelines considered for the current test-case are the following:

- 149** • Surroundings: buildings of height  $H_n$  have to be considered if they are within a distance of  $6H_n$  from  
**150** the area of interest;
- 151** • Vertical extension: an extension of  $5H_{max}$  above the tallest building is large enough to prevent artificial  
**152** acceleration of the flow;
- 153** • Extension in flow direction: outlet boundary is placed at a distance of  $15H_{max}$  behind the last building.

**154** In the purpose of this work, different wind directions were considered. Analogously to previous studies  
**155** [54, 55], the buildings of the Bovisa campus were rotated inside the domain when changing the flow direc-  
**156** tion, keeping the inflow plane perpendicular to the wind direction. To this end, all the sides were placed at  
**157** the maximum distance defined for the outlet.

**158** In Figure 5a the zone of interest is marked with a yellow line, the blue circle is the centre of the domain and  
**159** a red triangle indicates the location of the target building. In Figures 5b and 5c, the CAD model and the  
**160** mesh extent are displayed to demonstrate the dimensions of the domain and the geometry considered.

**161** The following step was the Wind Resource Assessment using experimental data recorded by an anemome-  
**162** ter placed in Bovisa Campus, and a further validation with a dataset provided by the Regional Environmental  
**163** Protection Agency (ARPA) [56]. Discrete directions were chosen with a step of  $30^\circ$ , resulting in 12 simula-  
**164** tions, each with its proper inlet conditions.

**165** A base-case was chosen to be analysed more in detail: the  $270^\circ$  (West to East) wind direction with an inlet  
**166** reference velocity of  $5.82m/s$  at  $17m$  of height. It was the most frequent wind direction, with almost 20%  
**167** relative frequency along the four years data records.

**168** Once boundaries were defined, the mesh was built in OpenFOAM®. A first simulation was run to charac-  
**169** terize the target point for the turbine positioning, chosen to be above the impinging side of a structure on  
**170** the target building. A representation of the turbine positioning is shown in Figure 6.

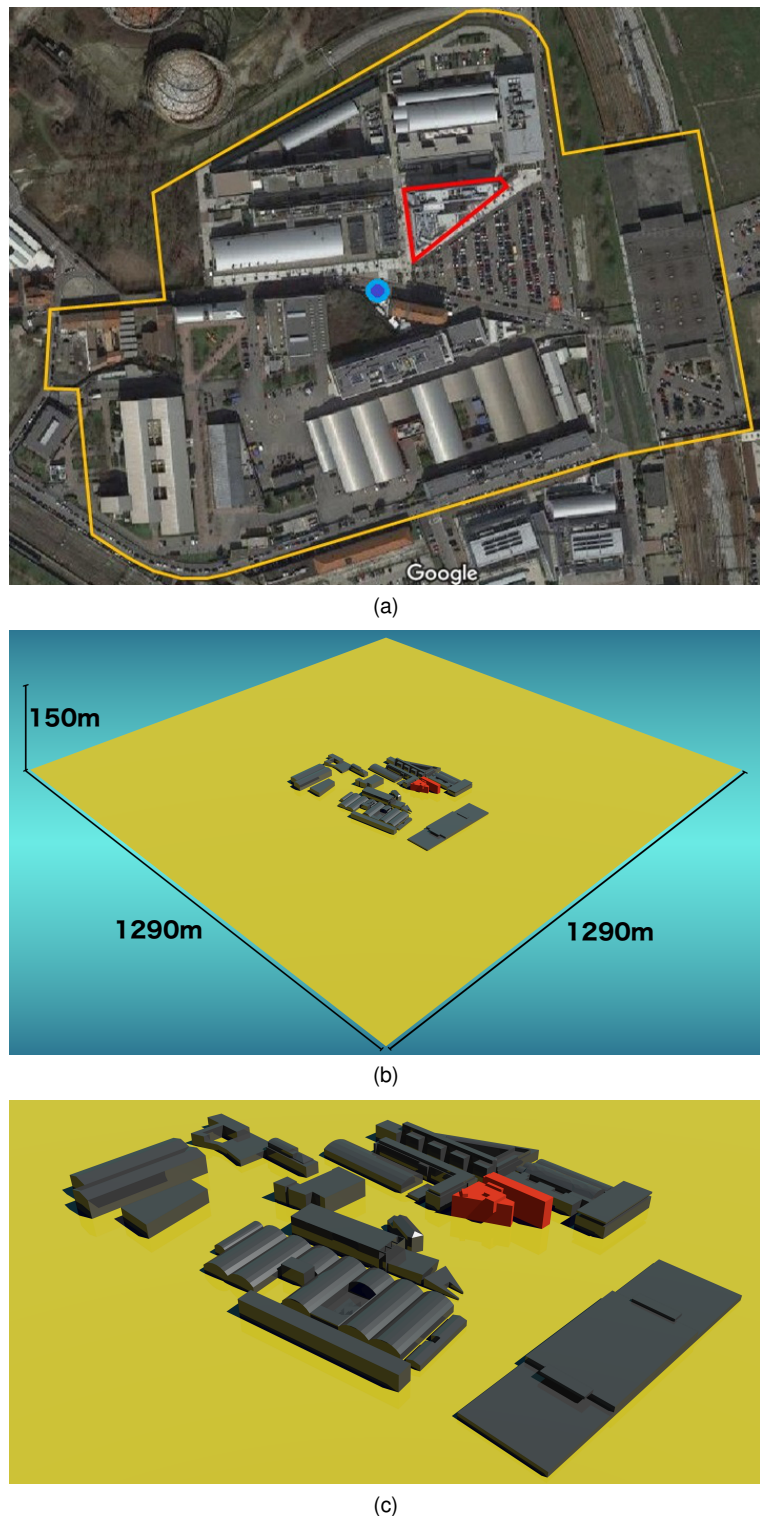


Figure 5: Zone of interest (Milan, Google Maps, 2019) (a), domain extent (b) and CAD model with the target building displayed in red (c) of the Bovisa campus.

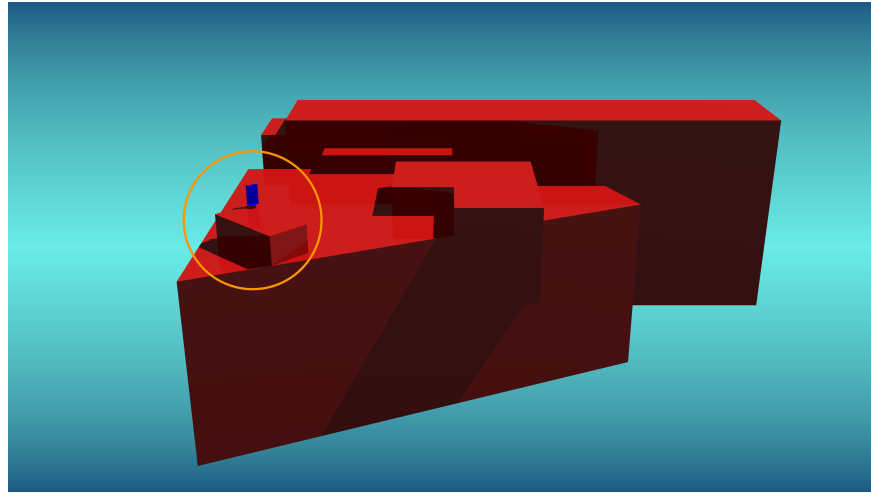


Figure 6: Turbine positioning on the target building.

## 2.4. Grid and GCI analysis

As for the grid distribution, the mesh is finest in the region of interest and close to the ground boundaries, then gradually decreasing in resolution. An approach with modular refinement using local boxes was used, with a local refinement for the region around the buildings and the highest level of refinement for the target building. This resulted in nearly 15 millions hexa cells. The grid distribution can be appreciated in Figure 7, for all the domain and for some strategic locations.

In the present work, two additional meshes were built, one coarser and one finer (refinement ratio  $r = 1.45$ ), as shown in Table 3; the relative errors of wind velocity and TKE between Coarse-Medium and Medium-Fine meshes were computed in order to assess the non-dependence of the result from the grid refinement.

Table 3: Percentage error of  $U$  and  $k$  for the three differently refined meshes.

Refinement	Cells [Millions]	TKE % Error	$U$ % Error
Coarse Mesh ( $f_3$ )	4,6	4%	2%
Medium Mesh ( $f_2$ )	15	5%	1.86%
Fine Mesh ( $f_1$ )	43	—	—

In addition, the GCI between refinement levels and convergence indexes for the two variables have been computed:

$$GCI = \frac{F_s |e|}{r^{p_c} - 1} \quad (4)$$

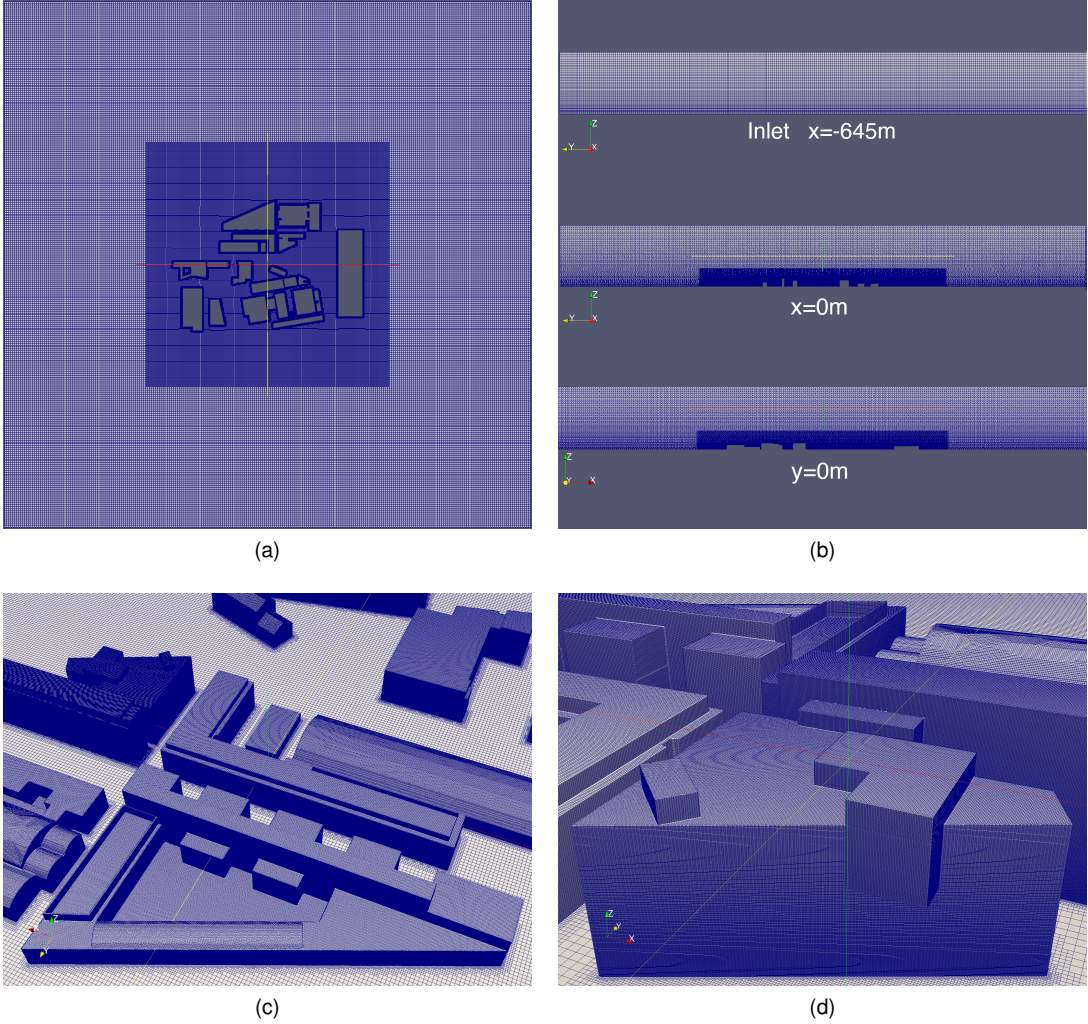


Figure 7: Computational mesh of the Bovisa campus on the domain ground (a), on the inlet and vertical  $x = 0\text{m}$  and  $y = 0\text{m}$  planes (b), on the buildings composing the campus (c) and on the target building (d).

where  $F_s$  is a safety factor:  $F_s = 1.25$ . The resulting GCIs are:

$$GCI_{12,TKE} = 2.7\% \quad GCI_{23,TKE} = 0.7\% \quad (5)$$

$$GCI_{12,U} = 3.2\% \quad GCI_{23,U} = 1.81\% \quad (6)$$

<sup>183</sup> Due to the computational effort requested by the finest mesh, the medium one was chosen considering the  
<sup>184</sup> limited discrepancy with the Fine mesh in terms of velocity and turbulent kinetic energy. Furthermore, the  
<sup>185</sup> value of  $y^+$  is ranging from 40 to 350 around the buildings for the Medium mesh and from 30 to 270 for the  
<sup>186</sup> Fine mesh, ensuring an appropriate level of refinement for the turbulence model.

<sub>188</sub> **3. Flow pattern around and over the target building**

<sub>189</sub> **3.1. Methods and Algorithms**

<sub>190</sub> For the twelve wind directions, the inlet conditions from Table 1 were employed:  $u_*$  was determined using  
<sub>191</sub> the available values of velocity for the considered wind direction. As for the  $k$  inlet profile, the coefficient  $C_1$   
<sub>192</sub> and  $C_2$  were retrieved through fitting to the semi-empirical relation of Brost and Wyngard [57]:

$$k(z) = \frac{1}{2} \left( \langle u'^2 \rangle + \langle v'^2 \rangle + \langle w'^2 \rangle \right) = \frac{u_*^2}{2} \left( 8.7 - 6 \frac{z}{h} \right) \quad (7)$$

<sub>193</sub> where  $h$  is the ABL height. For neutral stratification conditions the value of  $h$  can be deduced from the  
<sub>194</sub> following relation [58]:

$$\frac{hf_c}{u_*^2} \approx 0.33 \quad (8)$$

<sub>195</sub> where a mid-latitude value for the Coriolis parameter,  $f_c = 10^{-4} rad/s$ , can be considered [59].  
<sub>196</sub> The operation for determining  $u_*$ ,  $C_1$  and  $C_2$  was repeated per each wind direction considered. The area  
<sub>197</sub> around the Bovisa campus is characterized by a topology consisting of decommissioned fields, few low-rise  
<sub>198</sub> buildings, two extended railway junctions and a number of car parkings. Considering the reduced size of  
<sub>199</sub> the urban roughness elements,  $z_0$  was estimated to be equal to 0.4m [60, 61, 62].  
<sub>200</sub> Simulations were run in OpenFOAM®, employing the simpleFoam solver. Numerical schemes were set to  
<sub>201</sub> second order, bounded for gradient and divergence with the help of specific limiters defined conveniently  
<sub>202</sub> for the single terms. The geometric-algebraic multi-grid linear solver was employed for pressure, while the  
<sub>203</sub> other variables were treated with smoothed linear solvers using Gauss-Seidel smoothers.  
<sub>204</sub> Convergence was assessed monitoring both residuals and the value of three variables using six probes  
<sub>205</sub> positioned in different locations in the domain.

<sub>206</sub> **3.2. Base-Case Results**

<sub>207</sub> The aim of this Section is to extract the wind velocity distribution and use it as inlet condition to reliably  
<sub>208</sub> simulate the behavior of the wind turbine: an incoming wind distribution that differs from the undisturbed or  
<sub>209</sub> uniform profiles (namely the standard inlet profile used in wind turbines simulations), clearly represents a  
<sub>210</sub> different operating condition for the machine.

<sub>211</sub> To better interpret the level of disturbance of the flowfield around the buildings, the deviation parameter  $\delta_h$

212 is plotted in Figure 8a, at 5m of height. Whenever  $\delta_h$  is equal to 0, the comprehensive approach is em-  
213 ployed. A value close to 1 means that the flowfield is fully disturbed, leading to the application of the NLEV  
214 model. A value between 0 and 1 distinguishes the transition zone. As expected, the highest values of BIA  
215 are detected in correspondence of the wakes, the stagnation or deceleration zones generated by the urban  
216 environment.

217 In Figure 8b, a contour plot of relative velocity is shown for a vertical plane intersecting the target building. It  
218 can be observed that in proximity of the flat rooftops the fluid is accelerated with respect to the undisturbed  
219 flowfield. The intersection with the sampling plane is indicated by a white arrow: here the acceleration due  
220 to the presence of the obstacle itself was even more accentuated than in the upstream building, and the  
221 relative velocity was higher than the one registered in the undisturbed flowfield at the same height.

222 Analogous results were obtained when running the base-case with the same turbulent settings and param-  
223 eters on ANSYS Fluent R2019, whose relevant contour plots can be found in the supplementary material.

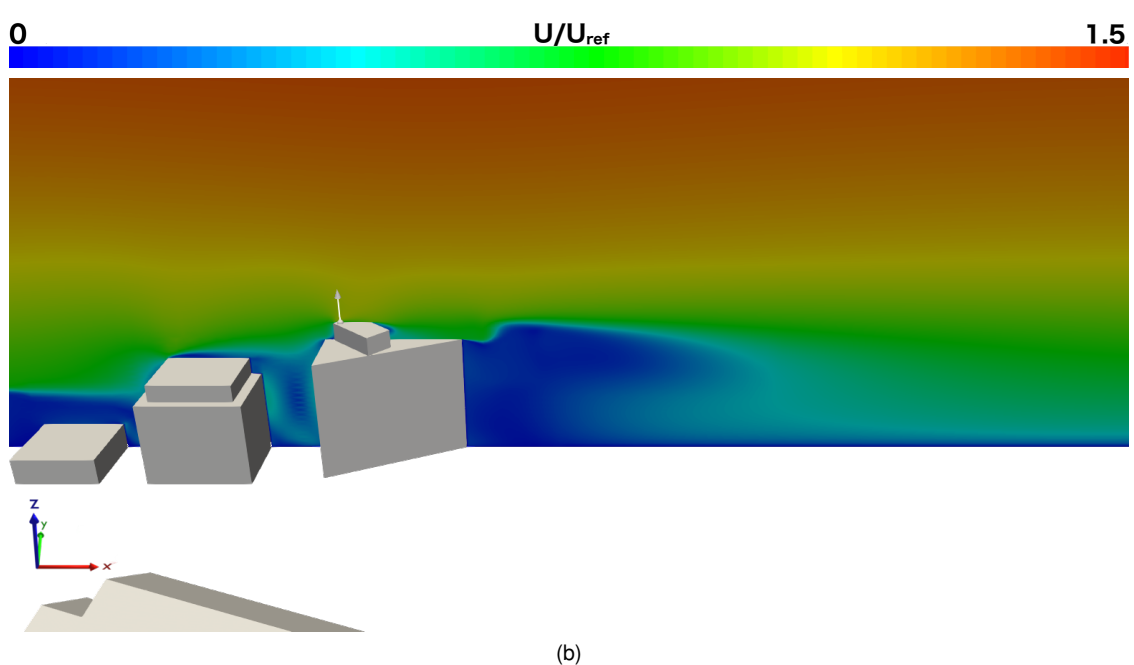
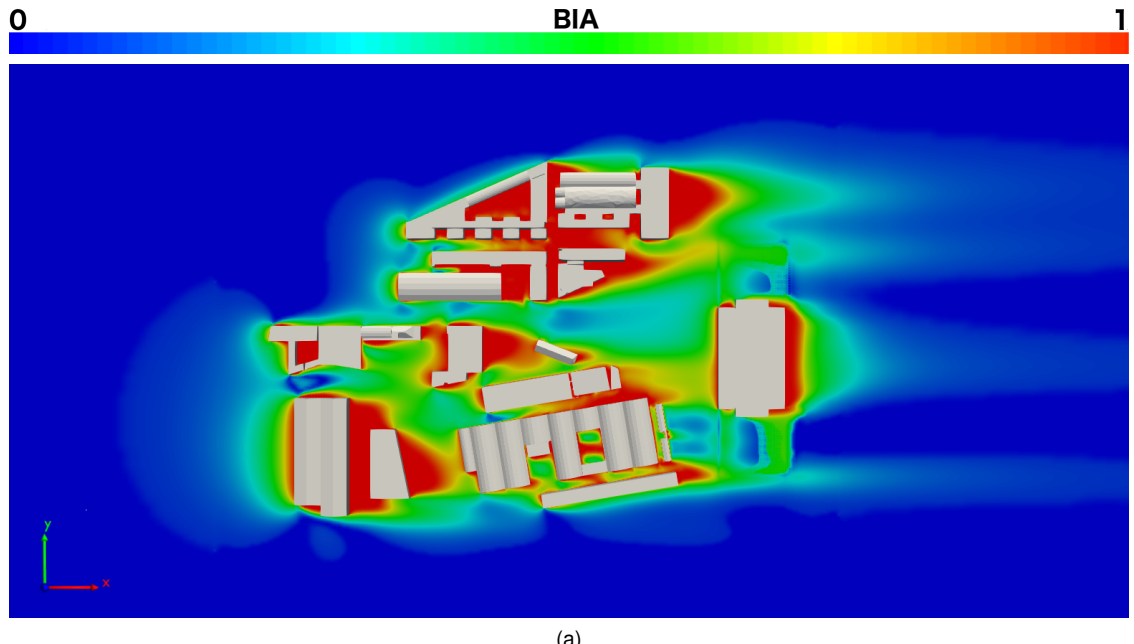


Figure 8: Contour plots of hybrid building influence area  $\delta_h$  at the horizontal plane  $z = 5m$  (a) and of relative velocity ( $U/U_R$ ) in the vertical plane, over the target building (b), for the base-case simulation. The wind is flowing from left to right.

<sub>224</sub> **3.3. Sensitivity Analysis**

<sub>225</sub> In Figure 9 all the relative velocity samples for each wind direction are provided, preceded by a legend for  
<sub>226</sub> direction and magnitude. The aim is to understand to which extent the obstacles affect the flow-stream  
<sub>227</sub> when a specific wind direction is under study.

<sub>228</sub> The sampling surface was rotated around the target point and was always perpendicular to the main wind  
<sub>229</sub> direction.

<sub>230</sub> The main results can be summarized as follows:

- <sub>231</sub> • in the  $0^\circ$ ,  $30^\circ$ ,  $60^\circ$  and  $330^\circ$  cases, the sample area on the target building was strongly influenced by  
<sub>232</sub> the presence of the surrounding environment.
- <sub>233</sub> • the  $120^\circ$  and  $150^\circ$  cases presented a very large undisturbed area upstream the target building, which  
<sub>234</sub> resulted as the only influence on the flow-stream.
- <sub>235</sub> • the remaining cases were influenced by low rising buildings that partially decelerated the stream-flow  
<sub>236</sub> before it reached the target building.

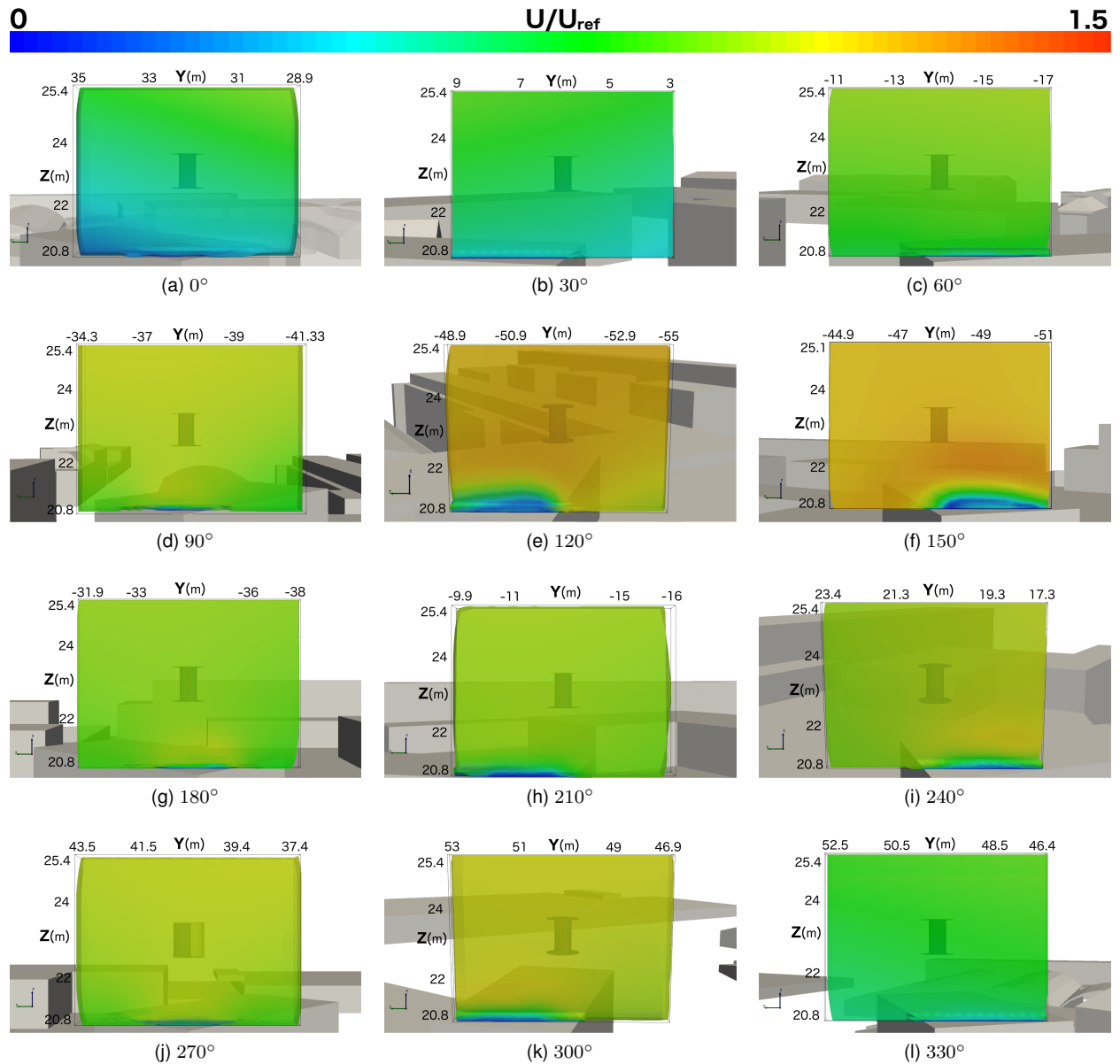
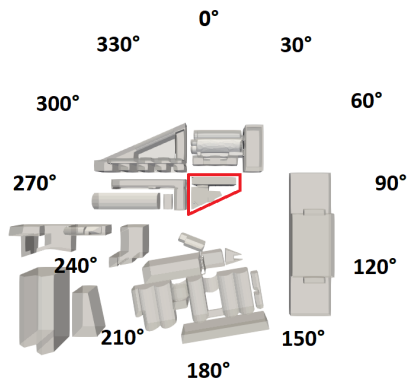


Figure 9: Normalized velocity  $U/U_{ref}$  distribution on sample surfaces perpendicular to the 12 considered wind directions.

<sup>237</sup> **3.4. Sampling for Turbine Simulations**

<sup>238</sup> The sampling of wind velocity distribution from the ABL mesh represents the link between meso (ABL) and  
<sup>239</sup> micro (Turbine) spatial scales. The ABL mesh region around the target location has been further refined  
<sup>240</sup> to reach the required resolution. Subsequently, the extracted wind velocity profiles were imposed as inlet  
<sup>241</sup> conditions for the Turbine simulation session.

<sup>242</sup> Sampling points were defined as follows: center point coordinates of the inlet surface of the Turbine mesh  
<sup>243</sup> (about 1300 points) were extracted and moved upstream of the target point for turbine positioning. Sampled  
<sup>244</sup> point data regarding velocity and turbulent characteristics were then used as inlet conditions for the turbine  
<sup>245</sup> inlet surface and applied in the respective cell center points 8 meters upwind the Turbine position.

<sup>246</sup> Two cases were selected for the turbine simulations: the 270° case, as it is the base-case of this work, and  
<sup>247</sup> the 0° case, considering it was the most negatively affected by the surrounding obstacles.

<sup>248</sup> In Figure 10a and 10b, the sample and the centreline plot of relative velocity are reported to highlight the  
<sup>249</sup> increase of wind velocity magnitude at the turbine's height, in respect to the reference one. The velocity  
<sup>250</sup> profile shows a gradient, that could affect the operating conditions and, consequently, the resulting effi-  
<sup>251</sup> ciency of the machine. In particular, in the lower central area ( $42m < y < 38m$  and  $20.8m < z < 21.4m$ ),  
<sup>252</sup> due to the presence of the roof, velocity tends to zero, while, above the aforementioned  $y$  limits, its value is  
<sup>253</sup> not null. This contributes to create a longitudinal gradient, almost symmetrical with respect to the  $z$  axis.

<sup>254</sup> Considering the 0° wind case, the sample and the centreline plot of relative velocity are displayed in Figures  
<sup>255</sup> 11a and 11b. In this location the wind velocity magnitude is lower than the one in the reference case, for  
<sup>256</sup> all the sample surfaces. Moreover, the velocity profile shows an even steeper gradient, varying along the  
<sup>257</sup> surface, with higher slope from the left to the right side of the sample.

<sup>258</sup> The results for the two wind conditions at 270° and 0° are used in the next Sections as inlet conditions for  
<sup>259</sup> the turbine simulation. The performance of the turbine at ideal and real conditions, with disturbed flowfield,  
<sup>260</sup> are compared to better understand the effect played by the urban environment on the potential energy  
<sup>261</sup> production.

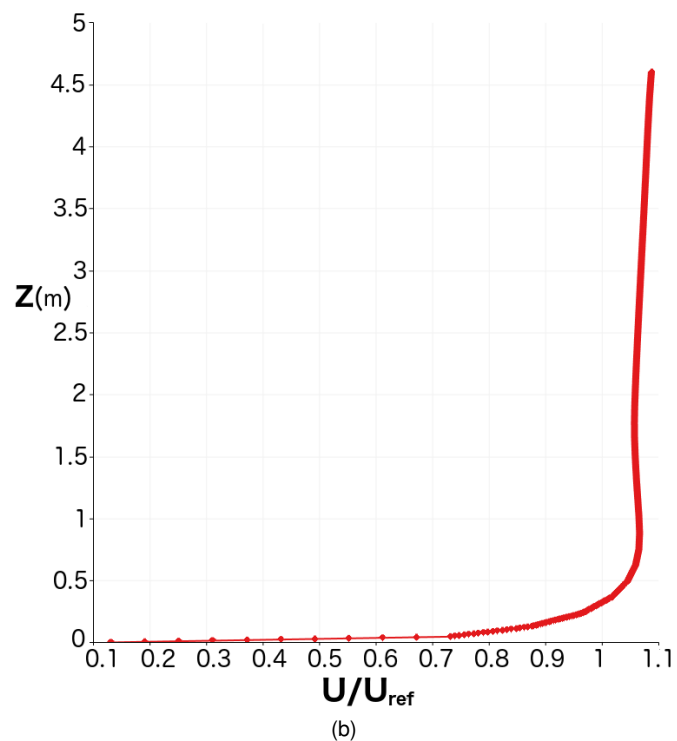
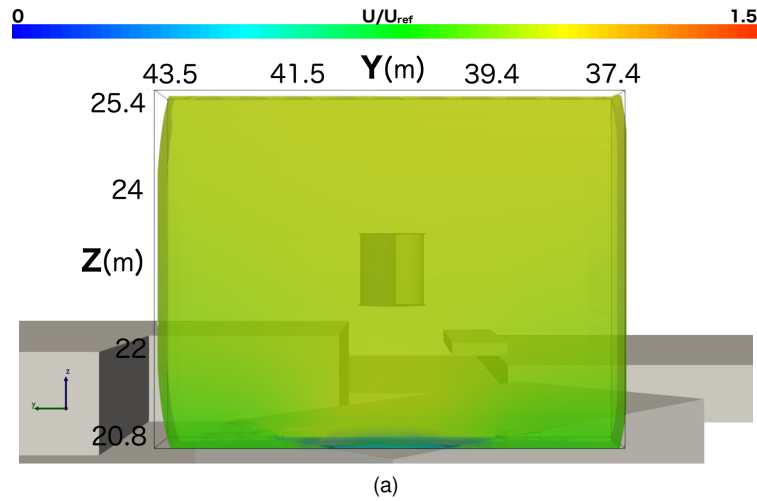


Figure 10: Contour plot (a) and centreline profile (b) of dimensionless wind velocity for the  $270^\circ$  wind direction case.

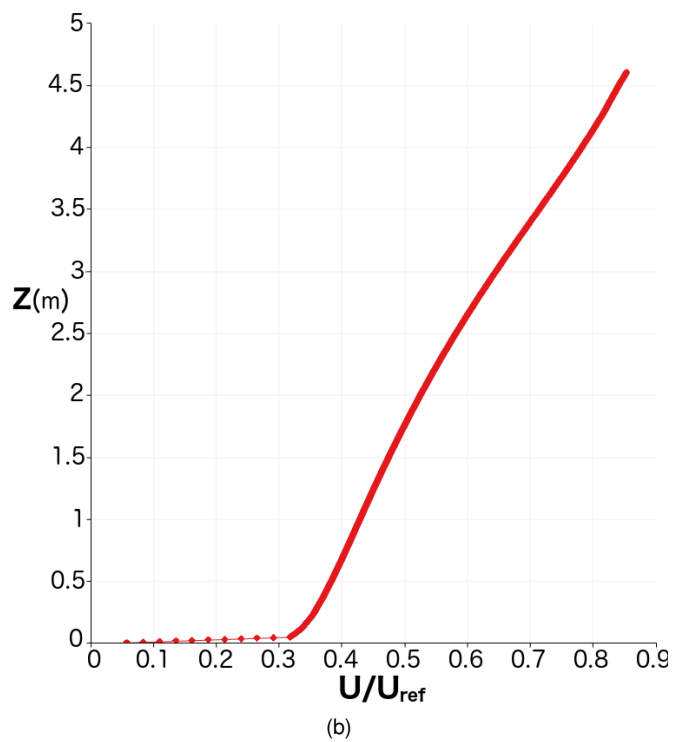
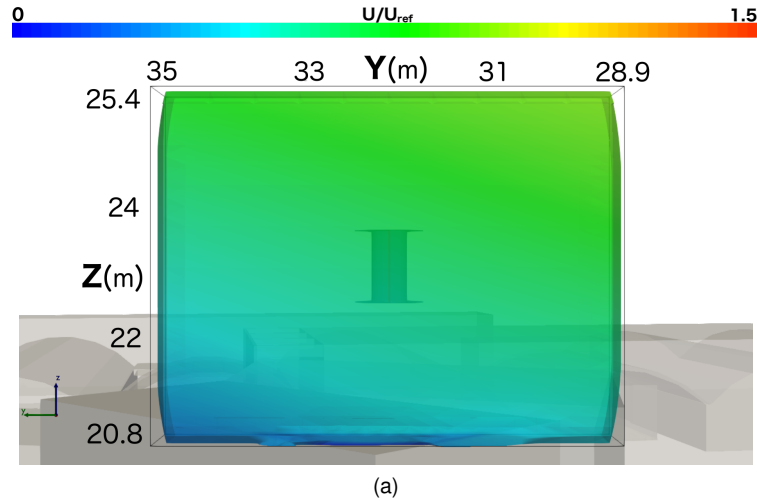


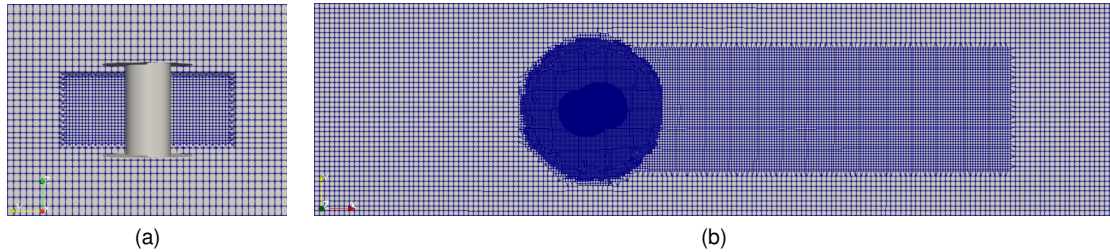
Figure 11: Contour plot (a) and centreline profile (b) of dimensionless wind velocity for the  $0^\circ$  wind direction case.

## 262 4. Turbine Analysis

263 The model of the Savonius turbine, previously studied at ideal conditions by Ferrari et al. [28], is investi-  
264 gated and the results compared with the ones obtained imposing the conditions for velocity and turbulent  
265 quantities resulting from the ABL simulations.

### 266 4.1. Mesh and Turbulence Modelling

267 The model built by Ferrari et al. [28] is used in the present work, with the dimensions of the Sandia wind  
268 tunnel [63]. The computational grid is shown in Figure 12, both in the vertical  $yz$  and horizontal  $xy$  planes.  
The inlet is positioned at  $x = -8m$  while the outlet at  $x = 15m$  downstream. The lateral boundaries extend



269 Figure 12: Computational mesh for the Savonius wind turbine, in the  $yz$  (a) and  $xy$  (b) planes.

270 for 6.1m, with the turbine placed in the symmetry plane. The mesh employed in this study is the one  
271 validated by Ferrari et al. [28] and Mereu et al. [29].

272 The choice of the turbulence model employed for this simulation is based on the sensitivity analysis of one  
273 and two-equation RANS models performed by Nasef et al. [64] and Ferrari et al. [28], with the selection of  
274 the SST  $k - \omega$  model. The choice of a model based on the SST  $k - \omega$  for the simulations of VAWTs was  
275 recently suggested, also, by Rezaeiha et al. [65]. This closure solves the Wilcox's original  $k - \omega$  model in  
276 the near-wall region together with a transformed  $k - \epsilon$  model in the far field, and blend them halfway [66].

277 As for the methods and algorithms, the same settings used in the previous work were employed [28, 29].

278 In particular, a transient solver for incompressible fluids on moving meshes was chosen, which uses the  
279 PIMPLE algorithm, namely pimpleDyMFoam.

280 The results of Ferrari et al. [28] had already been validated with the experimental data of Blackwell [26].  
281 Consequently mesh, numerical model and settings were considered reliable. For the purpose of this work,  
282 the most relevant results were the values of power coefficient  $C_p$ , which indicates the efficiency of a wind  
283 turbine.

284 From the comparison of the  $C_p$  trend of undisturbed (3D – CFD) and disturbed flows (Disturbed 0° and  
 285 270°) in Figure 13, it is evident the effect of the deviation of the velocity profiles, reported in Figure 10  
 286 (case 270°) and Figure 11 (case 0°). In particular, the flat profile with a value around  $1.1U_{ref}$  for the case  
 287 270° promotes the increase of  $C_p$  over the undisturbed case for higher  $TSR$ . The same influence can be  
 288 observed for the case at 0° that presents a velocity profile with a velocity ranging from 0.3 to  $0.9U_{ref}$  and  
 shows a  $C_p$  trend similar to the undisturbed one, but with lower values for all the  $TSR$  investigated.

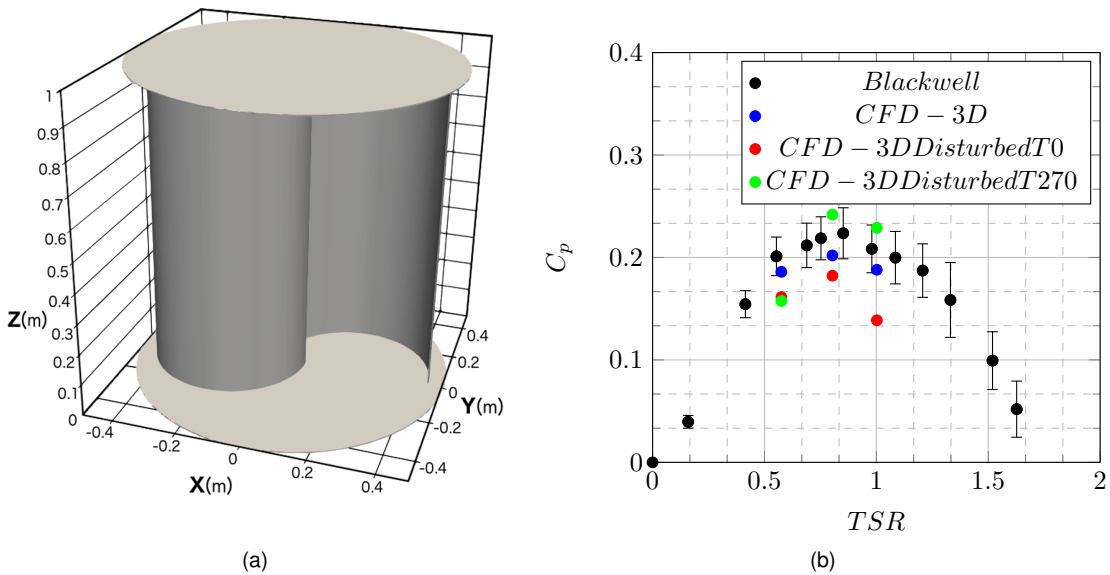


Figure 13: Savonius CAD model employed for the CFD simulation (a) and  $C_p$  obtained by 3D computational models and experimental data from Blackwell (b).

289  
 290 The reference-case for this part of the work is the optimal operating condition, at maximum efficiency (in  
 291 terms of power coefficient  $C_p$ ), which was determined to be at  $TSR = 0.81$ .  
 292 A first trial simulation with an uniform inlet was run in order to compare the so-obtained results with the  
 293 cases under study. This first simulation was labelled as reference-case. For the 270° and 0° wind directions,  
 294 the rotational speed was changed to reach the same tip speed ratio of the reference-case, by imposing an  
 295 undisturbed velocity, turbulence characteristics of the flow in terms of turbulent kinetic energy  $k$ , its specific  
 296 dissipation rate  $\omega$  and turbulent viscosity  $\mu_t$  computed on the sampled points in projected area of the turbine.

## 297 4.2. Results

298 The different efficiency in the three cases is now discussed. Table 4 reports the force coefficients (torque  
 299  $C_m$ , drag  $C_d$ , lift  $C_l$ ), the power coefficient  $C_p$  and the error on  $C_p$  with respect to the reference-case.

Table 4: Force/power coefficients and error on power coefficient for the  $270^\circ$  and  $0^\circ$  wind cases.

	<b>C<sub>m</sub></b>	<b>C<sub>d</sub></b>	<b>C<sub>I</sub></b>	<b>C<sub>p</sub></b>	<b>ΔC<sub>p</sub></b>
<b>Reference-case</b>	0.2686	1.0675	-0.9090	0.2176	
<b>270° case</b>	0.2986	1.2854	-0.8096	0.2418	+11%
<b>0° case</b>	0.2250	1.1670	-0.8426	0.1822	-16%

300 The subsequent plots were re-scaled using the undisturbed velocity for each wind direction. Figure 14  
 301 shows a comparison of relative velocity in form of contour (at  $x$  coordinate  $-1m$ ) and of plots over its  
 302 centreline ( $y = 0m$ ), between reference-case (dashed line) and  $270^\circ$  case (solid line). Dotted lines are  
 provided for the  $270^\circ$  case at  $y = 0.5m$  and  $y = -0.5m$ .

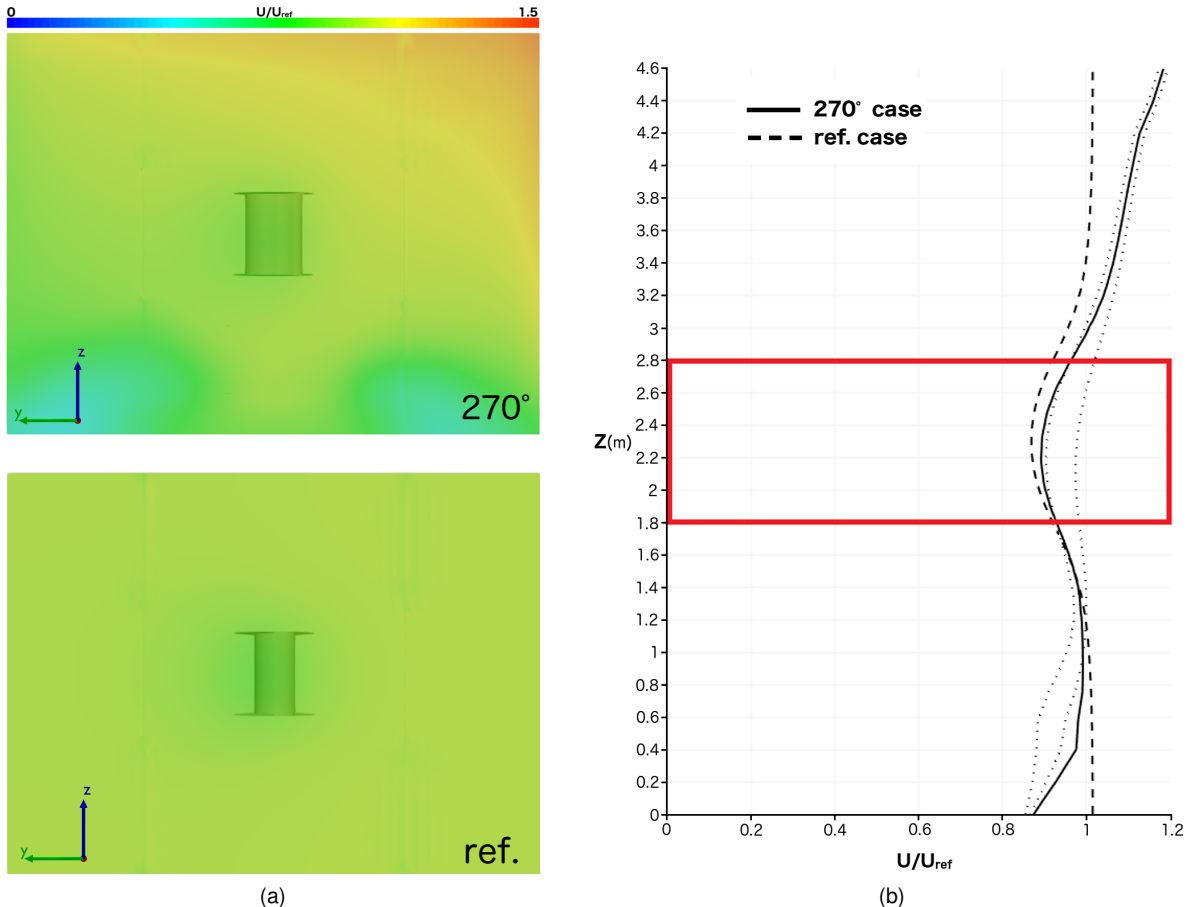


Figure 14: Comparison of relative velocity between the  $270^\circ$  case and the reference case at  $x = -1m$  in the form of contour plots (a) and profiles (b). The red rectangle represents the area of interest.

303  
 304 Figure 14 shows that the presence of the turbine led to an analogous effect in both cases. However, in the  
 305 zone of interest (red rectangle) the gradient of the sampled case was still evident and resulted in a higher  
 306 relative velocity at the top section of the machine. At the bottom of the turbine the relative velocity seemed

307 to be almost equal in the two cases.

308 A further investigation on the reason behind  $C_p$  increase involved the analysis of the local  $C_m$ . The turbine  
309 was subdivided in ten sections and local values of  $C_m$  were computed for both the current case and the  
reference-case; for the sake of simplicity, only four sections were considered (Figure 15a).

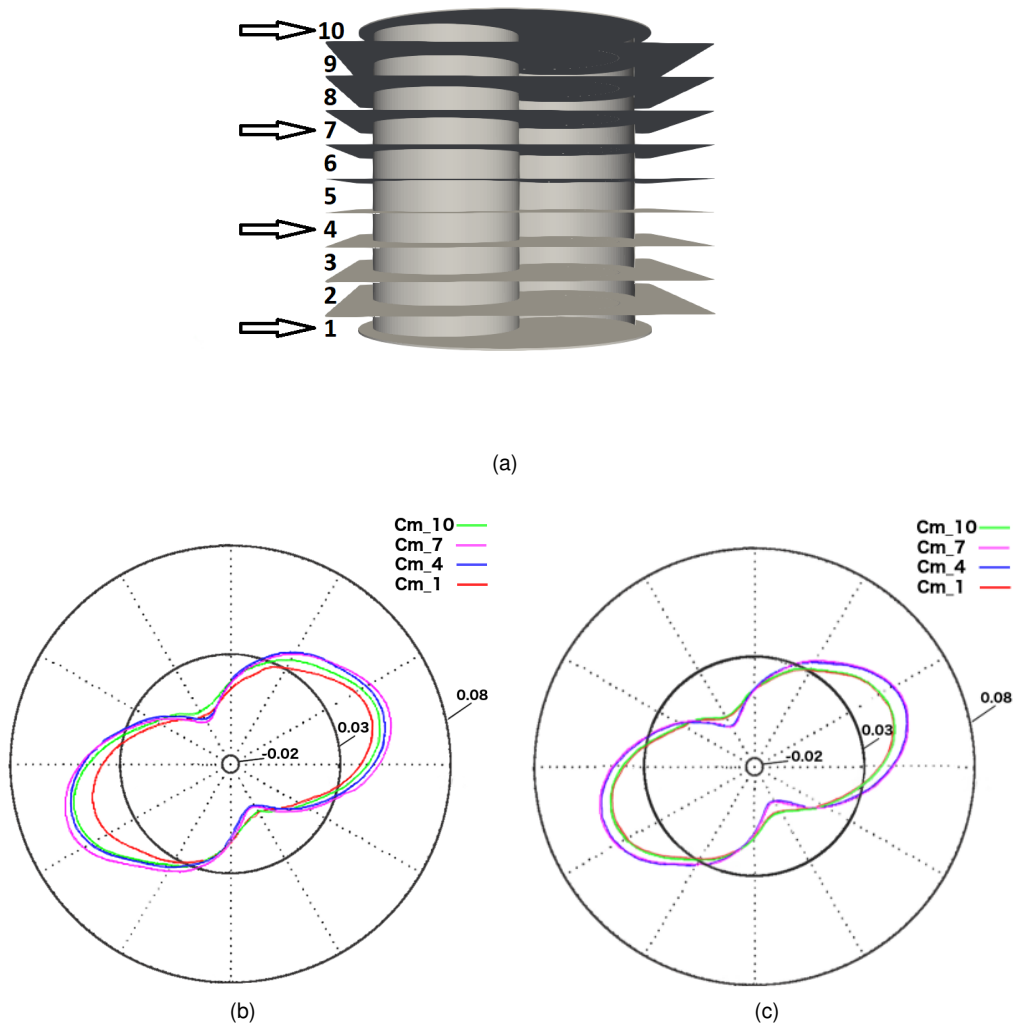


Figure 15: Four selected sections of the Savonius wind turbine (a), with the corresponding polar chart of torque coefficients  $C_m$  for the  $270^\circ$  wind direction case (b) and the reference case (c).

310  
311 From this analysis it followed that sections 1 to 3 had similar values of  $C_m$ , while the following sections  
312 showed higher values. In particular, in the reference-case, sections 1 to 5 have the same  $C_m$  values of  
313 the respective symmetrical sections 6 to 10; this behaviour was not observed in the sampled case. This  
314 highlighted how the peculiar shape of the velocity profile had a relevant impact on the local performance on

315 each section.

316 Figure 16, through relative velocity contours and a centerline plot, compares the reference-case and the  $0^\circ$  case. The presence of a gradient of velocity is once again evident in the contour plots in Figure 16a.

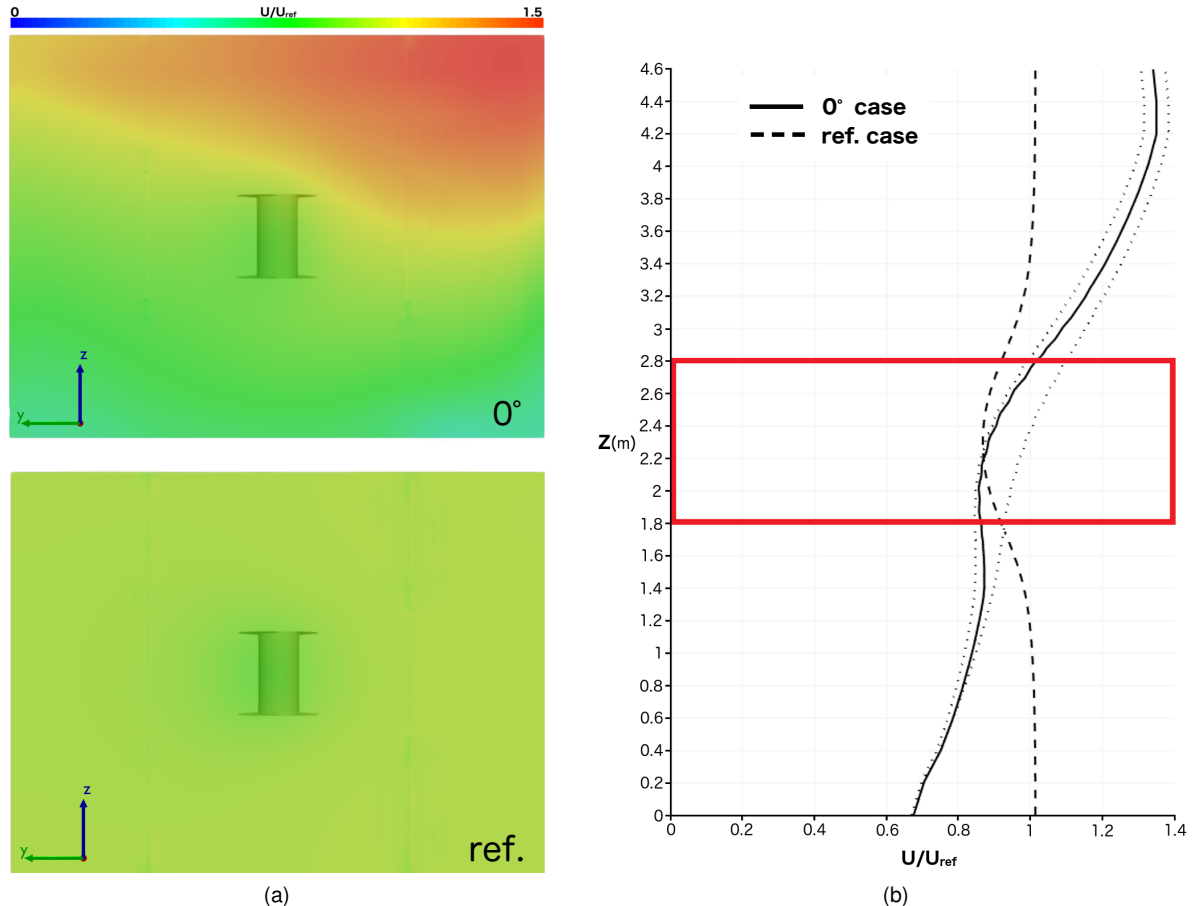
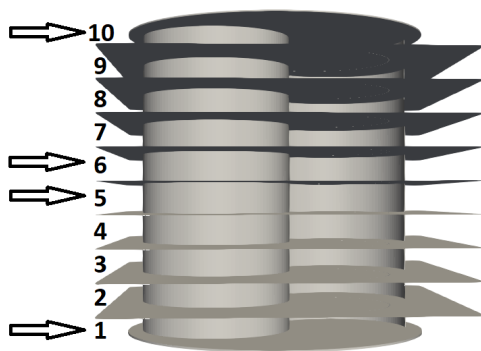
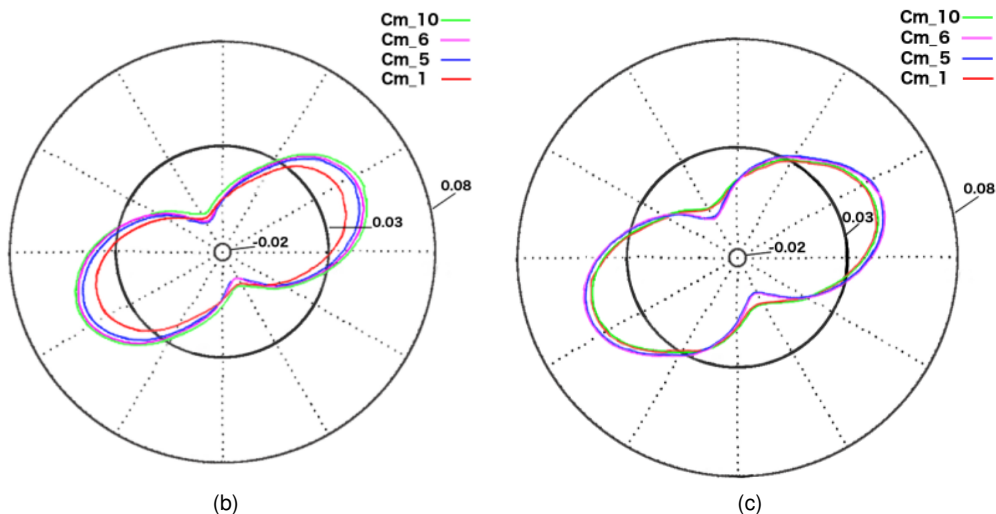


Figure 16: Comparison of relative velocity between the  $0^\circ$  case and the reference case at  $x = -1m$  in the form of contour plots (a) and profiles (b). The red rectangle represents the area of interest.

317  
318 Differently from the  $270^\circ$  case, the velocity profile showed an accentuated slope starting from the bottom of  
319 the domain, leading to a low relative velocity at the turbine's lower plate.  
320 The subdivision of the turbine in ten parts was applied, as previously done, in order to investigate local  
321 values of  $C_m$ ; the four chosen sections for this case are indicated in Figure 17a.  
322 From a detailed analysis of these data it was deduced that, from sections 1 to 6,  $C_m$  values were lower than  
323 the reference-case, while values from section 7 to 10 were higher, but still not enough to counter balance  
324 the decreased section.



(a)



(b)

(c)

Figure 17: Four selected sections of the Savonius wind turbine (a), with the corresponding polar chart of torque coefficients  $C_m$  for the  $0^\circ$  wind direction case (b) and the reference case (c).

325    **4.2.1. Energy Production**

326    Finally, an analysis on the turbine's energy production was performed to assess if the variation of  $C_p$  led  
327    to a relevant difference on the machine's output. Samples for the different orientations were evaluated in  
328    relation to the previous analysis and two groups of cases were set up:

- 329       • Group1: wind directions from  $90^\circ$  to  $300^\circ$ , whose relative velocity distribution on the centerline of the  
330       sampling face was very similar to the one of the  $270^\circ$  case; the  $C_p$  evaluated for the  $270^\circ$  case was  
331       assigned to this group.
- 332       • Group2: all wind directions involving near obstacles ( $330^\circ$ ,  $0^\circ$ ,  $30^\circ$ ,  $60^\circ$ ) whose velocity distribution  
333       resembled more the one of the  $0^\circ$  case; the  $C_p$  evaluated for the  $0^\circ$  case was assigned to this group.

334    The two groups have different impact on the result, due to the difference in both reference velocity ( $U_\infty$ )  
335    and relative frequency ( $f_i$ ) during the year. This led to a huge difference in the percentage of available  
power ( $\%P_{avail}$ ), as it can be seen in Table 5.

Table 5: Groups weight comparison on results.

	$\% \Delta C_p$	$\% P_{avail}$	$\% \Delta E$
Group1	+11%	97%	+10.78%
Group2	-16%	3%	-0.55%

336

337    The case study showed a total increase of 10.23% on the annual energy yield with respect to the reference-  
338    case, due to the combination of the two groups of results.

339    To underline the importance of the first part of the present work (employment of ABL turbulence models for  
340    determining the flow pattern), the same study on energy yield was made also using the reference velocity  
341    derived from the Wind Resource Assessment.

342    If no wind simulations had been performed, the turbine performance would have been computed on the  
343    basis of those wind velocity values, with a uniform inlet profile at the turbine's inlet and the same value  
344    of  $C_p$  for all wind directions. This would have led to an underestimation of the annual energy yield of  
345    11.53% with respect to the reference-case with inlet velocity estimated at the sample surfaces, or to an  
346    underestimation of 19.74% with respect to the turbine simulations with sampled profiles.

## **347 Conclusions**

348 This work stems from the awareness that district configuration severely impacts the exploitation of renew-  
349 able energy, affecting the local wind conditions and the performance of a urban wind turbine. Considering  
350 the high variability of the urban environment, this effect is strongly case-dependent and hard to be param-  
351 eterized. This further supports the deployment of computational fluid dynamics to comprehensively predict  
352 the flowfield in the area of interest.

353 The operating conditions of Savonius wind turbines should not be influenced by the horizontal change of  
354 wind direction. However, this is true only when ideal conditions and uniform inlet velocity distributions are  
355 involved. The deployment of CFD potential in this study has permitted to realistically predict the perfor-  
356 mance of the wind turbine under study, accounting for all the elements disturbing the flowfield. Without this  
357 analysis, all these observations could have been made only after the installation of the machine, leading,  
358 at least, to erroneous prediction in productivity or to inadequate positioning of the wind turbine. For this  
359 reason, this study suggests that even for small scale production with building integrated wind farms, a wind  
360 simulation campaign accounting for the local ABL and orography features should be employed to quantify  
361 the effective availability of wind resource and to optimize investments in urban-wind renewable source ex-  
362 ploitation.

363 Future improvements to the wind resource assessment could include the deployment of urban sensors for  
364 optimal data assimilation, as suggested by Sousa et al. [67], and the performing of wind gallery experiments  
365 to further assess the reliability of the numerical results.

## 366 References

- 367 [1] D. Mauree, E. Naboni, S. Coccolo, A.T.D. Perera, V. M. Nik, and J. Scartezzini. A review of assessment methods for the urban  
368 environment and its energy sustainability to guarantee climate adaptation of future cities. *Renewable and Sustainable Energy*  
369 *Reviews*, 112:733–746, 2019.
- 370 [2] G. Al Zohbi, P. Hendrick, and Ph. Bouillard. Evaluation of the impact of wind farms on birds: The case study of lebanon.  
371 *Renewable Energy*, (80):682–689, 2015.
- 372 [3] R. Mamani, N. Hackenberg, and P. Hendrick. Efficiency of high altitude on-shore wind turbines: Air density and turbulence  
373 effects—qollpana wind farm (bolivia). *proceedings*, (2(8)):487, 2018.
- 374 [4] A. Morabito and P. Hendrick. Pump as turbine applied to micro energy storage and smart water grids: A case study. *Applied*  
375 *Energy*, (241):557–579, 2019.
- 376 [5] G. de Oliveira e Silva and P. Hendrick. Pumped hydro energy storage in buildings. *Applied Energy*, (179):1242–1250, 2016.
- 377 [6] S. Giorgetti, G. Pellegrini, and G. Zanforlin. Cfd investigation on the aerodynamic interferences between medium-solidity darrieus  
378 vertical axis windturbines. *Energy Procedia*, (81):227–239, 2015.
- 379 [7] K. Kacprzak, G. Liskiewicz, and K. Sobczak. Numerical investigation of conventional and modified savonius wind turbines.  
380 *Renewable Energy*, (60):578–585, 2013.
- 381 [8] H. L. Bai, C. M. Chan, X. M. Zhu, and K. M. Li. A numerical study on the performance of a savonius-type vertical-axis wind  
382 turbine in a confined long channel. *Renewable Energy*, (139):102–109, 2019.
- 383 [9] J. Sousa and C. Gorlé. Computational urban flow predictions with bayesian inference: Validation with field data. *Building and*  
384 *Environment*, 154:13–22, 2019.
- 385 [10] F. Toja-Silva, T. Kono, C. Peralta, O. Lopez-Garcia, and J. Chen. A review of computational fluid dynamics (cfd) simulations of  
386 the wind flow around buildings for urban wind energy exploitation. *Journal of Wind Engineering and Industrial Aerodynamics*,  
387 (180):66–87, 2018.
- 388 [11] C. G. Sánchez, J. van Beeck, and C. Gorlé. Predictive large eddy simulations for urban flows: Challenges and opportunities.  
389 *Building and Environment*, 139:146–150, 2018.
- 390 [12] O. Temel and J. van Beeck. Two-equation eddy viscosity models based on the monin–obukhov similarity theory. *Applied*  
391 *Mathematical Modelling*, (42):1–16, 2017.
- 392 [13] O. Temel, S. Porchetta, and J. Bricteux, L. van Beeck. Rans closures for non-neutral microscale cfd simulations sustained with  
393 inflow conditions acquired from mesoscale simulations. *Applied Mathematical Modelling*, (53):635–652, 2018.
- 394 [14] P. Richards and R. Hoxey. Appropriate boundary conditions for computational wind engineering models using the k–epsilon  
395 turbulence model. *Journal of Wind Engineering and Industrial Aerodynamics*, (46(47)):145–153, 1993.
- 396 [15] A. Parente and C. Benocci. On the rans simulation of neutral abl flows. 2010.
- 397 [16] R. Longo, M. Ferrarotti, C. Garcia Sanchez, M. Derudi, and A. Parente. Advanced turbulence models and boundary conditions  
398 for flows around different configurations of ground-mounted buildings. *Journal of Wind Engineering and Industrial Aerodynamics*,  
399 (167):160–182, 2017.
- 400 [17] R. Longo, M. Fürst, , M. Ferrarotti, M. Deurdi, and A. Parente. Cfd dispersion study based on a variable schmidt formulation for  
401 flows around different configurations of ground-mounted buildings. *Building and Environment*, 154:336–347, 2019.
- 402 [18] A. Parente, C. Gorlè, J. van Beeck, and C. Benocci. Improved k–e model and wall function formulation for the rans simulation of  
403 abl flows. *Journal of Wind Engineering and Industrial Aerodynamics*, (99):267–278, 2011.

- 404 [19] M. Pontiggia, M. Derudi, V. Busini, and R. Rota. Hazardous gas dispersion: A cfd model accounting for atmospheric stability  
 405 classes. *Journal of Hazardous Materials*, 171(1 - 3):739 – 747, 2009.
- 406 [20] F.S. Lien, W.L. Chen, and M.A. Leschziner. Low reynolds-number eddy-viscosity modelling based on non-linear stress-  
 407 strain/vorticity relations. *Engineering Turbulence Modelling and Experiments 3*, 1996.
- 408 [21] T. J. Craft, B. E. Launder, and K. Suga. Development and application of a cubic eddyviscosity model of turbulence. *International  
 409 Journal of Heat and Fluid Flow*, 17:108–115, 1995.
- 410 [22] J. Ehrhard and N. Moussiopoulos. On a new non-linear turbulence model for simulating flows around building shaped structures.  
 411 *Journal of Wind Engineering and Industrial Aerodynamics*, (88):91–99, 2000.
- 412 [23] A. Parente, C. Gorlè, J. van Beek, and C. Benocci. A comprehensive modelling approach for the neutral atmospheric boundary  
 413 layer (abl): Consistent inflow conditions, wall function and turbulence model. *Boundary-Layer Meteorology*, 2011.
- 414 [24] W. Tian, Z. Mao, B. Zhang, and Y. Li. Shape optimization of a savonius wind rotor with different convex and concave sides.  
 415 *Renewable Energy*, (117):287–299, 2018.
- 416 [25] A. Vergaerde, T. De Troyer, L. Standaert, J. Kluczewska-Bordier, A. Pitance, A. Immas, F. Silvert, and M. C. Runacres. Ex-  
 417 perimental validation of the power enhancement of a pair of vertical-axis wind turbines. *Renewable Energy*, (146):181–187,  
 418 2020.
- 419 [26] B.F. Blackwell, R.E. Sheldahl, and L.V. Feltz. *Wind Tunnel Performance Data for Two- and Three-Bucket Savonius Rotor*. 1977.
- 420 [27] N.H. Mahmoud, A.A. El-Haroun, E. Wahba, and M.H. Nasef. An experimental study on improvement of savonius rotor perfor-  
 421 mance. *Alexandria Engineering Journal*, (51):19–25, 2012.
- 422 [28] G. Ferrari, D. Federici, P. Schito, F. Inzoli, and R. Mereu. Cfd study of savonius wind turbine: 3d model validation and parametric  
 423 analysis. *Renewable Energy*, 105:722–734, 2017.
- 424 [29] R. Mereu, D. Federici, G. Ferrari, P. Schito, and F. Inzoli. Parametric numerical study of savonius wind turbine interaction in a  
 425 linear array. *Renewable Energy*, 113:1320–1332, 2017.
- 426 [30] E. Antar and M. Elkhoury. Parametric sizing optimization process of a casing for a savonius vertical axis wind turbine. *Renewable  
 427 Energy*, (136):127–138, 2019.
- 428 [31] L. Sumei, P. Wuxuan, Z. Xingwang, Z. Hao, C. Xionglei, L. Zhengwei, and C. Qingyan. *Influence of surrounding buildings on  
 429 wind flow around a building predicted by CFD simulations*. Number 140. 2018.
- 430 [32] J. Srebric, M. Heidarnejad, and j. Liu. Building neighborhood emerging properties and their impacts on multi-scale modeling of  
 431 building energy and airflows. *Building and Environment*, (91):246–262, 2015.
- 432 [33] A. L. Pisello, J. E. Taylor, X. Xu, and F Cotana. Inter-building effect: Simulating the impact of a network of buildings on the  
 433 accuracy of building energy performance predictions. *Building and Environment*, (58):37–45, 2012.
- 434 [34] K. C. Anup, J. Whale, and T. Urmee. Urban wind conditions and small wind turbines in the built environment: A review. *Renewable  
 435 Energy*, (113):268–283, 2019.
- 436 [35] T. Sharpe and G. Proven. Crossflex: Concept and early development of a true building integrated wind turbine. *Energy and  
 437 Buildings*, (42):2365–2375, 2010.
- 438 [36] J. Franke, A. Hellsten, H. Schlunzen, and B. Carissimo. *Best Practice Guideline for the CFD Simulation Of Flows in the Urban  
 439 Environment*. University of Hamburg Centre of Marine and Atmospheric Sciences, 2007.
- 440 [37] M. Pontiggia, G. Landucci, V. Busini, M. Derudi, M. Alba, M. Scaioni, S. Bonvicini, V. Cozzani, and R. Rota. Cfd model simulation  
 441 of lpg dispersion in urban areas. *Atmospheric Environment*, 45:3913–3923, 2011.
- 442 [38] V. Busini and R. Rota. Influence of the shape of mitigation barriers on heavy gas dispersion. *Journal of Loss Prevention in the*

- 443        *Process Industries*, 29:13–21, 2014.
- 444        [39] P. Ouro, B. Fraga, N. Viti, A. Angeloudis, T. Stoesser, and C. Gualtieri. Instantaneous transport of a passive scalar in a turbulent  
445        separated flow. *Environmental Fluid Mechanics*, 2017.
- 446        [40] H.K. Versteeg and W. Malalasekera. *An introduction to computational fluid dynamics - the finite volume method*. Pearson, 2007.
- 447        [41] W. Bauer, W. Haag, and D.K. Hennecke. Accuracy and robustness of nonlinear eddy viscosity models. *International Journal of  
448        Heat and Fluid Flow*, 21:312–319, 2000.
- 449        [42] H.G. Kim, V.C Patel, and C.M. Lee. Numerical simulation of wind flow over hilly terrain. *Journal of Wind Engineering and  
450        Industrial Aerodynamics*, 87:45–60, 2000.
- 451        [43] K.W. Ayotte, D. Xu, and P. A. Taylor. The impact of turbulence closure schemes on predictions of the mixed spectral finite-  
452        difference model for flow over topography. *Boundary-Layer Meteorology*, 68:1–33, 1994.
- 453        [44] M. Balogh, A. Parente, and C. Benocci. Rans simulation of abl flow over complex terrains applying an enhanced k- $\epsilon$  model and  
454        wall function formulation: Implementation and comparison for fluent and openfoam. *Journal of Wind Engineering and Industrial  
455        Aerodynamics*, (104-106):360–368, 2012.
- 456        [45] A. Parente, R. Longo, and M. Ferrarotti. *CFD boundary conditions, turbulence models and dispersion study for flows around  
457        obstacles*. VKI LS 2017-01, 2017.
- 458        [46] A. Parente, R. Longo, and M. Ferrarotti. *Turbulence model formulation and dispersion modelling for the CFD simulation of flows  
459        around obstacles and on complex terrains*. VKI LS 2019-03, 2019.
- 460        [47] R. Longo, , Marco Ferrarotti, and A. Parente. Cubic turbulence closures and dispersion models for flows around different  
461        configurations of ground-mounted buildings. ETMM11 - 11th International ERCOFTAC Symposium on Engineering Turbulence  
462        Modelling and Measurements, 2016.
- 463        [48] R. Longo, A. Bellemans, M. Ferrarotti, M. Derudi, and A. Parente. A new turbulent schmidt number formulation based on  
464        the local turbulence level. ETMM12 - 12th International ERCOFTAC Symposium on Engineering Turbulence Modelling and  
465        Measurements, 2018.
- 466        [49] C. Peralta, A. Parente, M. Balogh, and C. Benocci. Rans simulation of the atmospheric boundary layer over complex terrain with  
467        a consistent k-epsilon model formulation. *Proceedings of the 6th International Symposium on Computational Wind Engineering  
468        (CWE2014)*, (Hamburg, Germany):236–237, 2014.
- 469        [50] H. Montazeri and B. Blocken. Cfd simulation of wind-induced pressure coefficients on buildings with and without balconies:  
470        Validation and sensitivity analysis. *Building and Environment*, 60:137–149, 2013.
- 471        [51] Y. Tominaga, A. Mochida, T. Shirasawa, R. Yoshie, H. Kataoka, K. Harimoto, and T. Nozu. Cross comparisons of cfd results of  
472        wind environment at pedestrian level around a high-rise building and within a building complex. page 257–266. *Journal of Asian  
473        Architecture and Building Engineering*, 2004.
- 474        [52] J. Franke, C. Hirsh, A. Jensen, H. Krus, M. Schatzmann, P. Westbury, S. Miles, J. Wisse, and N. Wright. *Reccomandations on  
475        the Use of CFD in Wind Engineering*. University of Hamburg Centre of Marine and Atmospheric Sciences, 2004.
- 476        [53] Y. Tominaga, A. Mochida, R. Yoshie, H. Karaoka, T. Nozu, Y. Masaru, and T. Shirasawa. Aij guidelines for practical applications  
477        of cfd to pedestrian wind environment around buildings. *Journal of Wind Engineering and Industrial Aerodynamics*, (96):1749–  
478        1761, 2008.
- 479        [54] C. Gorlè, ClaraGarcia-Sánchez, and G. Iaccarino. Quantifying inflow and rans turbulence model form uncertainties for wind  
480        engineering flows. *Journal of Wind Engineering and Industrial Aerodynamics*, (144):202–212, 2015.
- 481        [55] C. García-Sánchez, D. A. Philips, and C. Gorlé. Quantifying inflow uncertainties for cfd simulations of the flow in downtown

- 482       oklahoma city. *Building and Environment*, (78):118–129, 2014.
- 483   [56] ARPA. Regional environmental protection agency, 2019.
- 484   [57] R. A. Brost and J. C. Wyngaard. A model study of the stably stratified planetary boundary layer. *Journal of the Atmospheric Sciences*, 35(8):1427–1440, 1978.
- 485
- 486   [58] A Bechmann. *Large-Eddy Simulation of Atmospheric Flow over Complex Terrain*. PhD thesis, Technical University of Denmark,
- 487       2006.
- 488   [59] A. Parente and M. Longo, R. Ferrarotti. *CFD boundary conditions, turbulence models and dispersion study for flows around obstacles*, volume CFD for atmospheric flows and wind engineering - hardcover - VKI LS 2017-01. 2017.
- 489
- 490   [60] S. Liu, W. Pan, H. Zhang, X. Cheng, Z. Long, and Q. Chenm. Cfd simulations of wind distribution in an urban community with a
- 491       full-scale geometrical model. *Building and Environment*, (117):11–23, 2017.
- 492   [61] B. Blocken, T Stathopoulos, and J. Carmeliet. Cfd simulation of the atmospheric boundary layer: wall function problems. *Atmospheric Environment*, (41):238–252, 2007.
- 493
- 494   [62] J. Wieringa. Updating the davenport roughness classification. *Wind Eng. Ind. Aerodyn.*, (41):357–368, 1992.
- 495   [63] B. Blackwell, R. Sheldahl, and L. Feltz. Wind tunnel performance data for two and three bucket savonius rotors. *J. Energy*, pages
- 496       160–164, 1977.
- 497   [64] M. Nasef, W. El-Askary, H. Abdel-Hamid, and H. Gad. Evaluation of savonius rotor performance: static and dynamic studies. *J. Wind Eng. Ind. Aerodyn.*, (123):1–11, 2013.
- 498
- 499   [65] A. Rezaeiha, H. Montazeri, and B. Blocken. On the accuracy of turbulence models for cfd simulations of vertical axis wind
- 500       turbines. *Energy*, 180:838–857, 2019.
- 501   [66] F.R. Menter. Zonal two equation k-omega turbulence models for aerodynamic flows. *24th Fluid Dynamics Conference*, 1993.
- 502   [67] J. Sousa, C. G. Sánchez, and C. Gorlé. Improving urban flow predictions through data assimilation. *Building and Environment*,
- 503       132:282–290, 2018.